Topography, structural and exhumation history of the Admiralty Mountains region, northern Victoria Land, Antarctica

Maria Laura Balestrieri, Valerio Olivetti, Federico Rossetti, Cécile Gautheron, Silvia Cattò, Massimiliano Zattin

Geoscience Frontiers 11 (2020) 1841–1858

HOSTED BY

Contents lists available at ScienceDirect

Geoscience Frontiers

journal homepage: www.elsevier.com/locate/gsf

Research Paper

Topography, structural and exhumation history of the Admiralty Mountains region, northern Victoria Land, Antarctica

Maria Laura Balestrieri [a], Valerio Olivetti [b,*], Federico Rossetti [c], Cécile Gautheron [d], Silvia Cattò [b], Massimiliano Zattin [b]

[a] Istituto di Geoscienze e Georisorse, Consiglio Nazionale delle Ricerche, Sede Secondaria Firenze, via G. La Pira 4, 50121, Firenze, Italy
[b] Dipartimento di Geoscienze, Università di Padova, Padova, Italy
[c] Dipartimento di Scienze, Università degli Studi Roma 3, Roma, Italy
[d] GEOPS, Univ. Paris Sud, CNRS Université Paris-Saclay, 91405, Orsay, France

ARTICLE INFO

Handling Editor: Stijn Glorie

Keywords:
Antarctica
Thermochronology
Transantarctic mountains
Rift margin uplift

ABSTRACT

The Admiralty Mountains region forms the northern termination of the northern Victoria Land, Antarctica. Few quantitative data are available to reconstruct the Cenozoic morpho-tectonic evolution of this sector of the Antarctic plate, where the Admiralty Mountains region forms the northern termination of the western shoulder of the Mesozoic–Cenozoic West Antarctica Rift System. In this study we combine new low-temperature thermochronological data (apatite fission-track and (U-Th-Sm)/He analyses) with structural and topography analysis. The regional pattern of the fission-track ages shows a general tendency to older ages (80–60 Ma) associated with shortened mean track-lengths in the interior, and younger fission-track ages clustering at 38–26 Ma with long mean track-lengths in the coastal region. Differently from other regions of Victoria Land, the younger ages are found as far as 50–70 km inland. Single grain apatite (U-Th-Sm)/He ages cluster at 50–30 Ma with younger ages in the coastal domain. Topography analysis reveals that the Admiralty Mountains has high local relief, with an area close to the coast, 180 km long and 70 km large, having the highest local relief of >2500 m. This coincides with the location of the youngest fission-track ages. The shape of the area with highest local relief matches the shape of a recently detected low velocity zone beneath the northern TAM, indicating that high topography of the Admiralty Mountains region is likely sustained by a mantle thermal anomaly. We used the obtained constraints on the amount of removed crustal section to reconstruct back-eroded profiles and calculate the erosional load in order to test flexural uplift models. We found that our back-eroded profiles are better reproduced by a constant elastic thickness of intermediate values (Te = 20–30 km). This suggests that, beneath the Admiralty Mountains, the elastic properties of the lithosphere are different with respect to other TAM sectors, likely due to a stationary Cenozoic upper mantle thermal anomaly in the region.

1. Introduction

The Transantarctic Mountains (TAM) form the uplifted rift shoulder of the West Antarctic Rift System (WARS). The TAM are located along the transition region between two different lithosphere structures: the presumably hot and thin, extended continental domain of the WARS and the cold and thick East Antarctic craton (Dalziel, 1992; Salvini et al., 1997). The TAM stretch N–S for ca. 3500 km from the Weddell Sea region to the Pacific coast of Northern Victoria Land (NVL) in the north (Fig. 1a, inset). In NVL the TAM is widest, being ca. 400 km in width compared to an average of 100–300 km.

Several models have been proposed to explain uplift of the TAM (for a compilation see Lawrence et al., 2006). They include delayed phase changes in the crust (eclogite to basalt or quartz-eclogite to granulite; Smith and Drewry, 1984), simple shear extension (Fitzgerald et al., 1986), different types of flexure models (Stern and ten Brink, 1989; Bott and Stern, 1992; ten Brink and Stern, 1992; ten Brink et al., 1993), plastic (Chery et al., 1992) and elastic (van der Beek et al., 1994) necking models, transform-flank uplift (ten Brink et al., 1997), and collapse of a high plateau, with thick crust providing buoyancy (Studinger et al., 2004;

* Corresponding author.
E-mail address: valerio.olivetti@unipd.it (V. Olivetti).
Peer-review under responsibility of China University of Geosciences (Beijing).

https://doi.org/10.1016/j.gsf.2020.01.018
Received 24 May 2019; Received in revised form 25 October 2019; Accepted 26 January 2020
Available online 19 February 2020

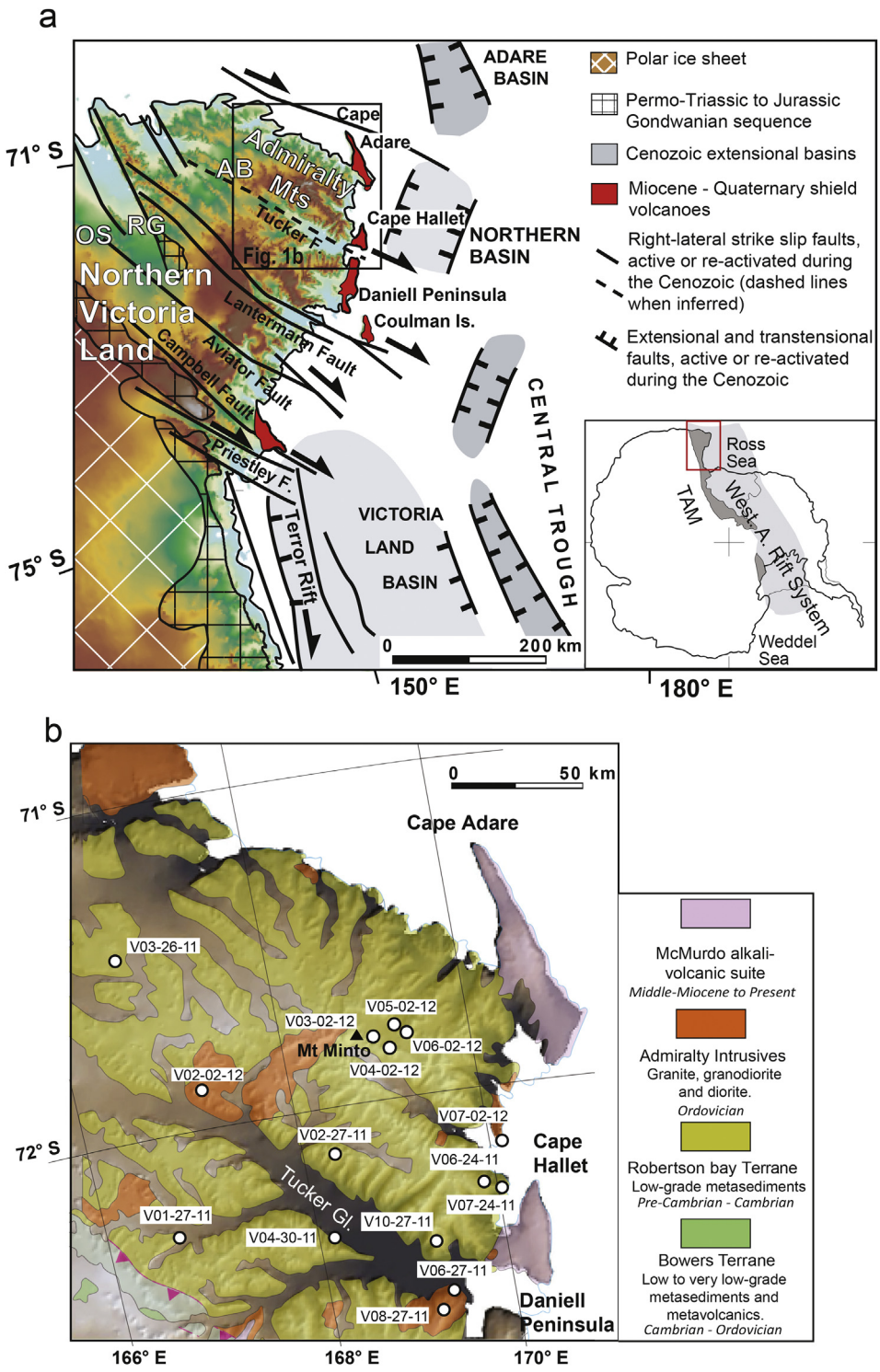

Fig. 1. (a) Topographic relief map of the northern Victoria Land showing the main topographic and bathymetric features and principal Cenozoic tectonic structures. The black square frames the study area. AB: Admiralty Block; RG: Rennick Graben; OS: Outback Shoulder. Modified from Fitzgerald (1992); Salvini et al. (1997); Storti et al. (2008); Olivetti et al. (2018). (b) Admiralty Mountains region simplified geological map with sample localities. Map after GANOVEX Team (1987).

Bialas et al., 2007). A central question in the debate about the origin of the TAM is whether the uplift is provided by thermal buoyancy due to perturbed upper mantle temperatures (e.g., ten Brink et al., 1997), or by thickened crust (Studinger et al., 2004). The recent increase in available geophysical data (i.e. Graw et al., 2016; Brenn et al., 2017) constrains the thermal and mechanical state of the crust and upper mantle, providing new input for geodynamic models. Despite these improvements, integration of new geophysical data with tectonic constraints is limited, because of the limited field and geological data that constrain the style and timing of deformation.

The Admiralty Mountains area in NVL constitutes the northwest termination of the TAM. This area, positioned on the western shoulder of the Northern Basin (Fig. 1a), shows some peculiar characteristics: (i) the large extent of high topography; (ii) Alpine-style morphological features; (iii) lack of a Permo-Triassic to Jurassic Gondwanian terrestrial sequence (Armienti and Baroni, 1999; Lisker et al., 2006, and references therein),

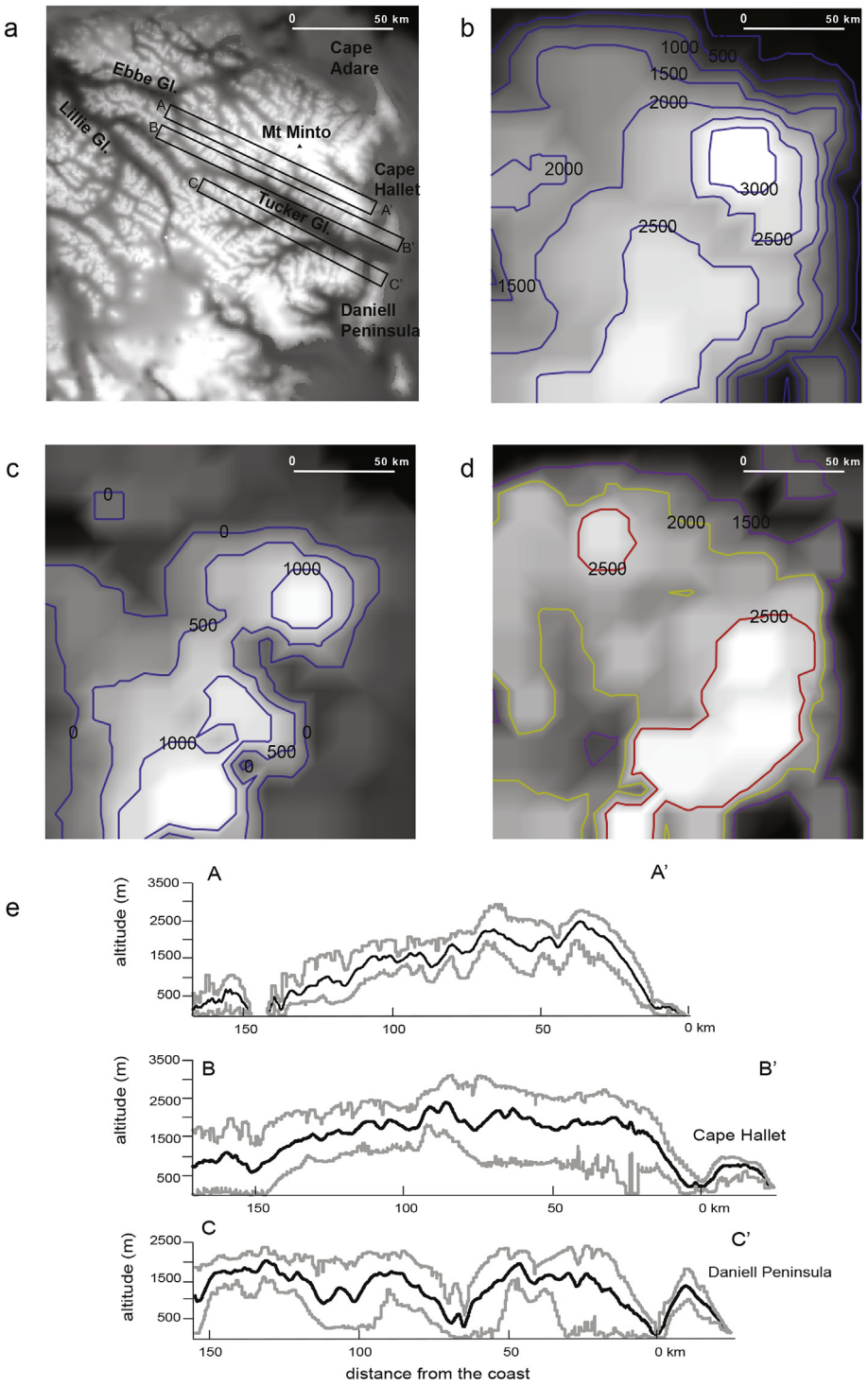

Fig. 2. Topography analysis of Admiralty Block. (a) Bedmaps2 by the British Antarctic Survey (Fretwell et al., 2013), with traces of the extracted swath profiles; (b) summit level map; (c) base level map; (d) local relief map; (e) swath profiles showing the min, mean and max elevations.

and (iv) an impressive coastal belt of north-south aligned Miocene–Quaternary shield (alkaline) volcanoes (LeMasurier and Thomson, 1990) (Fig. 1). For these reasons the Admiralty Mountains area was proposed to be the location of the most recent, since the Miocene, tectonic deformation, exhumation and morphogenesis throughout the TAM (Faccenna et al., 2008). In particular, Faccenna et al. (2008) inferred that the morphotectonic setting and Cenozoic magmatism of the Admiralty Mountains area cannot be explained by flexural uplift only, and a dynamic contribution of mantle upwelling is sustaining the present topography and controlling volcanism in the region. Recently, Graw et al. (2016) highlighted the presence of a low-velocity zone in the sub-lithospheric mantle beneath the northern TAM, extending from 160 to ~60 km depths, and attributed to rift-related decompression melting during Cenozoic extension.

Our study is conceived on integration of field- and laboratory-based investigations. A revised picture of the present-day topography of the Admiralty Mountains region is combined with new (i) structural data addressed to refine the brittle structural architecture of the region; and

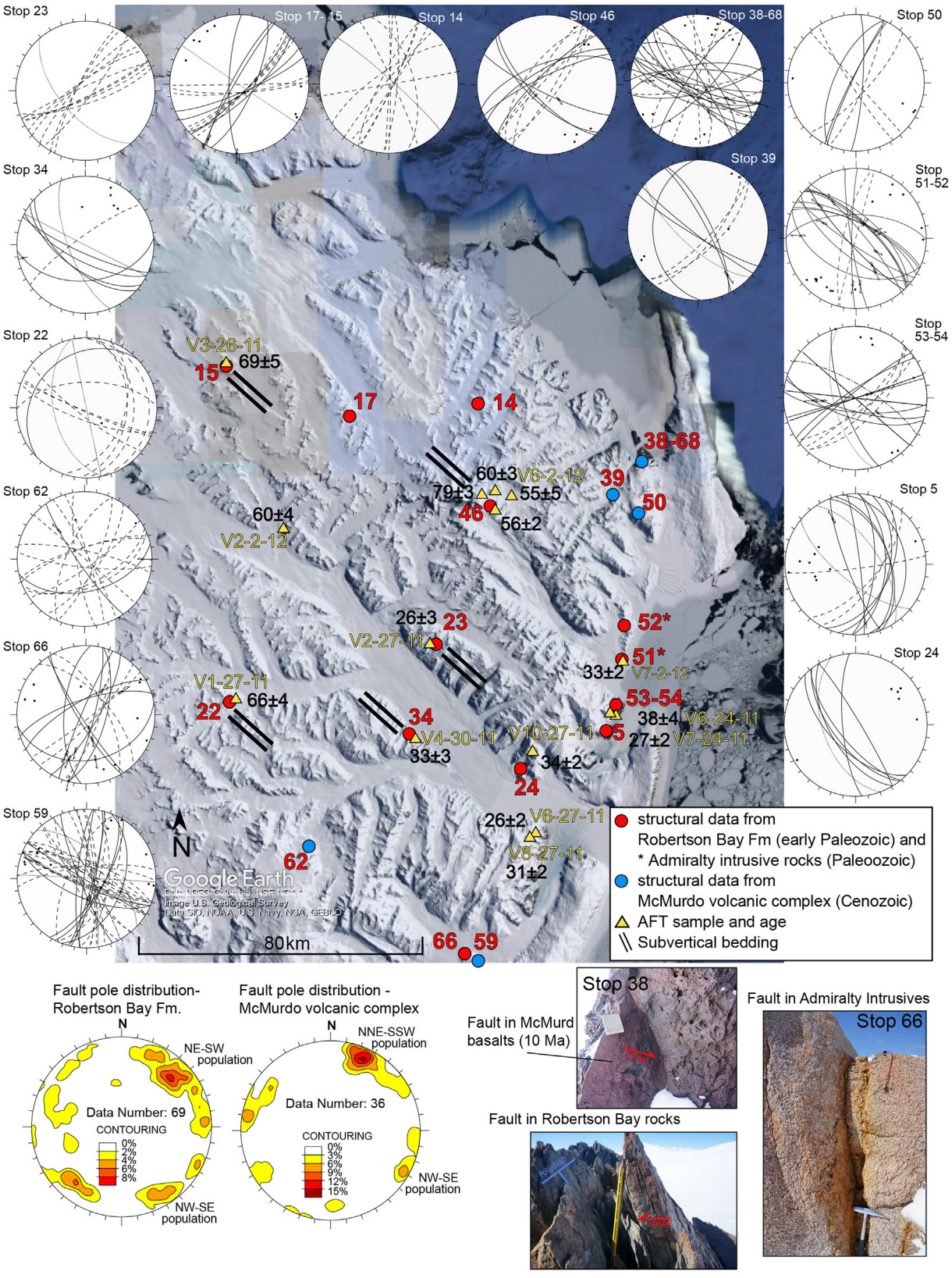

Fig. 3. Google Earth view of the study area. Fault planes and striae are shown on lower hemisphere, Schmidt projection. Cumulative data from Robertson Bay formation and Cenozoic volcanic rock are also shown.

Table 1
Apatite fission-track data.

Sample	Site	Latitude (S)	Longitude (E)	El. **(m)**	ρ_d	n_d	ρ_s	n_s	ρ_i	n_i	n_g	P(χ^2) **(%)**	Central age (Ma±1σ)	U (μg/g)	Lm±1σ (μm)	s.d. (μm)	n_{TINTs}	Dpar (μm)	s.d.
V06_24_11	Cape Christie	72°18′30.39″	169°54′24.17″	1098	3.2	1906	9.6	678	15.6	1104	22	<1	**38.1 ± 4.0**	68.1	14.1 ± 0.2	1.8	72	2.3(86)	0.6
V07_24_11	Cape Christie	72°19′21.80″	169°55′46.36″	40	3.2	1855	4.6	536	9.7	1115	31	85.5	**27.1 ± 1.5**	43.6	14.2 ± 0.2	1.4	34	1.3(124)	0.3
V03_26_11	Robinson Heights	71°25′30.08″	166°52′31.47″	1841	3.2	1869	10.4	817	8.6	676	25	9.0	**69.1 ± 4.6**	33.6	13.2 ± 0.3	2.02	57	2.0(100)	0.3
V01-27-11	Mt. Pearson	72°16′20.71″	166°40′ 56.47″	1749	3.3	1958	11.3	850	10.1	765	25	67.5	**65.9 ± 3.5**	40.01	12.3 ± 0.9	2.3	100	2.4(95)	0.4
V02_27_11	Freimanis Gl.	72°7′55.13″	168° 30′3.98″	2176	3.3	1932	2.8	258	6.1	555	24	11.3	**26.2 ± 2.6**	25.5	–	–	–	2.5(87)	1.1
V06_27_11	Purvis Peak	72°38′15.80″	169°17′5.73″	944	3.3	3266	2.7	296	5.9	638	27	18.4	**26.5 ± 2.2**	25.3	13.6 ± 0.6	1.6	7	1.8(94)	0.5
V08_27_11	Purvis Peak	72°38′43.29″	169°08′49.98″	2217	3.3	1945	2.9	360	5.5	696	28	81.1	**30.6 ± 2.1**	19.7	14.7 ± 0.3	1.1	17	1.9(117)	0.3
V10_27_11	Mt. Trident	72°25′37.72″	169°17′13.23″	1897	3.4	1983	8.7	666	16.0	1219	24	7.4	**33.7 ± 2.2**	52.6	14.5 ± 0.4	2.0	32	1.9(96)	0.3
V04_30_11	Stevenson Peak	72°21′58.47″	168°15′35.85″	151	3.1	1829	6.2	249	10.5	421	24	90.1	**32.9 ± 2.7**	45.7	14.8 ± 0.6	0.8	2	2.0(94)	0.2
V02_02_12	Rastorfer Gl.	71°52′19.30″	167°14′59.72″	1565	3.2	1880	31.9	1207	30.7	1161	22	<1	**59.6 ± 3.7**	112.3	13.8 ± 0.2	2.1	100	2.6(88)	0.3
V03_02_12[a]	Mt Minto	71°48′36.97″	168°54′5.12″	2646	11.0	2861	4.9	889	17.1	3107	30	99	**55.7 ± 2.4**	21.5	13.4 ± 0.3	1.9	69	1.9(90)	0.3
V04_02_12[a]	Mt Minto	71°46′35.22″	168°48′47.83″	3484	10.8	2817	5.9	1144	14.3	2766	30	91	**79.2 ± 3.2**	16.2	13.6 ± 0.2	1.6	111	1.9(156)	0.3
V05_02_12[a]	Mt Minto	71°45′50.66″	168°55′3.15″	2061	10.7	2772	6.7	948	20.9	2967	30	92	**60.3 ± 2.5**	22.9	13.4 ± 0.3	1.7	63	1.9(125)	0.3
V06_02_12	Mt Minto	71°45′54.18″	169°59′ 21.00″	1831	3.2	1893	10.2	567	10.5	588	29	1.1	**54.9 ± 4.6**	39.2	13.2 ± 0.3	2.4	69	2.8(80)	0.4
V07_02_12	Helm Point	72°11′08.52″	167°14′59.72″	80	3.1	1842	10.0	551	17.0	937	27	44.5	**32.9 ± 1.9**	64.2	14.4 ± 0.2	1.3	59	2.2(59)	0.3

Notes - Ages determined by external detector method using a zeta value for dosimeter CN5, analyst Balestrieri $\zeta = 360 \pm 11$, analyst Cattò $\zeta = 355 \pm 4$ (referred to Fish Canyon Tuff and Durango apatite standards, Hurford, 1990). El (m): sample elevations in metres; ρ_d, ρ_i: standard and induced track densities measured on mica external detectors; ρ_s: spontaneous track densities on internal mineral surfaces, track densities are given in 10^5 tracks cm^{-2}; n_d, n_i and n_s: number of tracks on external detectors and on mineral surfaces; n_g: number of counted mineral grains; P(χ^2): (χ^2) probability (Galbraith, 1981); Central age calculated using TRACKKEY program (Dunkl, 2002); Lm: mean length of confined tracks length distribution ± standard error, s.d.: standard deviation, n_{TINTs}: number of measured lengths; only TINTs (tracks reached by the etching because they intercept a surface track, Bhandari et al., 1971) were measured, as recommended by Ketcham (2005). Dpar: mean etch pit diameter parallel to the c-axis and number of total measured Dpar for sample; samples were irradiated in the Lazy Susan facility of the Triga Mark II reactor of the LENA, University of Pavia, Italy.

[a] Samples irradiated at the Radiation Centre of Oregon University, USA (analyst Cattò).

Table 2
Apatite (U-Th-Sm)/He data.

Sample	^{4}He (ncc)	Mass Ca (mg)	U (ppm)	Th (ppm)	Sm (ppm)	Th/U ratio	eU (ppm)	R_s (μm)	F_T	Uncorrected age (Ma)	Corrected age (Ma±1σ)
V06-24-11A	0.837	2.88	19.9	33.7	22.3	1.7	28	45.0	0.69	24.7	35.8 ± 2.1
V06-24-11B	0.888	2.32	16.6	64.4	171.3	3.9	32	46.6	0.74	22.1	29.8 ± 1.8
V06-24-11C	0.694	1.42	13.1	23.8	11.2	1.8	19	35.3	0.65	30.5	46.9 ± 2.8
V06-24-11D	1.968	5.86	53.3	57.4	29.0	1.1	67	63.9	0.78	24.3	31.1 ± 1.9
V06-24-11E	1.038	7.64	27.8	17.5	27.5	0.6	32	56.0	0.75	26.7	35.6 ± 2.1
V07-24-11A	1.550	1.06	36.6	19.8	30.7	0.5	41	35.0	0.61	35.6	58.4 ± 3.5
V07-24-11B	0.295	2.61	0.4	21.8	4.2	57.0	6	50.0	0.75	54.1	72.1 ± 4.3[a]
V07-24-11C	0.072	1.64	8.0	38.3	19.4	4.8	17	38.5	0.67	33.1	49.4 ± 3.0
V07-24-11D	1.751	1.24	28.9	36.2	38.6	1.3	38	42.0	0.67	54.2	80.9 ± 4.9
V07-24-11E	0.050	2.73	8.8	26.0	45.1	3.0	15	48.3	0.08	27.7	338.2 ± 20.3[a]
V03-26-11B	0.196	3.74	8.2	1.9	10.6	0.2	9	42.5	0.67	82.2	122.7 ± 7.4[a]
V03-26-11C	0.10	1.77	9.6	19.2	75.1	2.0	14	43.3	0.68	51.7	76.1 ± 4.6
V03-26-11D	0.680	2.47	1.3	9.8	19.6	7.5	4	50.2	0.72	159.8	221.9 ± 13.3[a]
V03-26-11E	0.450	0.94	68.9	10.6	11.7	0.2	71	35.5	0.61	51.3	84.2 ± 5.1
V03-26-11F	0.352	2.19	−0.2	2.3	0.8		0	44.3		627.9	923.4 ± 54.4[a]
V01-27-11A	0.033	1.85	6.8	9.4	4.9	1.4	9	40.3	0.68	30.6	45.0 ± 2.7
V01-27-11B	0.152	1.56	50.1	4.3	23.9	0.1	51	34.9	0.65	24.5	37.7 ± 2.3
V01-27-11C	0.324	1.65	35.4	191.5	35.4	5.4	81	40.5	0.67	33.1	49.4 ± 3.0
V01-27-11D	0.063	2.00	4.1	29.9	32.1	7.3	11	39.0	0.68	45.6	67.1 ± 4.0[a]
V01-27-11E	0.123	1.89	13.8	93.8	22.5	6.8	36	45.3	0.69	28.2	40.9 ± 2.5
V02-27-11A	0.094	1.99	14.6	44.7	55.8	3.1	25	40.3	0.66	30.4	46.0 ± 2.8
V02-27-11B	0.105	1.64	19.3	18.1	6.1	0.9	24	34.9	0.65	37.0	57.0 ± 3.4
V02-27-11E	0.957	2.00	181.3	380.9	9.0	2.1	273	43.7	0.68	29.2	42.9 ± 2.6
V06-27-11A	0.221	1.20	16.0	17.3	93.9	1.1	20	34.2	0.66	87.4	132.4 ± 7.9
V06-27-11D	0.391	0.44	24.3	28.8	157.2	1.2	31	28.0	0.56	99.7	178.0 ± 10.7[a]
V06-27-11E	0.104	2.26	19.4	33.0	140.8	1.7	27	42.1	0.69	30.4	44.0 ± 2.6
V08-27-11A	0.137	2.00	15.5	46.9	48.5	3.0	27	42.1	0.67	42.1	62.8 ± 3.8
V08-27-11B	0.059	1.84	10.5	26.2	24.1	2.5	17	32.4	0.58	29.1	50.2 ± 3.0
V10-27-11A	0.016	1.47	2.9	9.0	2.2	3.1	5	33.5	0.66	26.5	40.1 ± 2.4
V10-27-11B	0.287	1.16	61.0	101.5	36.0	1.7	85	37.6	0.65	27.8	42.8 ± 2.6
V10-27-11C	0.079	1.59	11.3	19.7	14.3	1.8	16	36.0	0.66	40.7	61.7 ± 3.7
V04-30-11A	0.224	1.07	17.8	62.6	57.0	3.5	33	32.6	0.58	56.2	96.9 ± 5.8[a]
V04-30-11B	0.199	1.56	42.8	112.5	23.8	2.6	70	40.0	0.65	23.7	36.4 ± 2.2
V04-30-11C	0.035	1.90	3.7	4.9	1.5	1.3	5	34.5	0.61	59.9	98.3 ± 5.9[a]
V04-30-11D	0.388	0.78	55.8	76.0	20.2	1.4	74	32.0	0.57	43.4	76.1 ± 4.6[a]
V02-02-12A	0.551	1.85	148.1	33.8	61.9	0.2	156	43.5	0.70	29.1	41.5 ± 2.5
V02-02-12B	0.476	2.52	136.5	29.3	61.9	0.2	144	41.9	0.67	27.3	40.8 ± 2.4
V02-02-12C	0.426	2.16	134.4	35.6	53.3	0.3	143	41.9	0.67	24.6	36.7 ± 2.2
V02-02-12D	0.250	1.21	87.6	24.2	53.7	0.3	93	35.4	0.62	22.1	35.6 ± 2.1
V02-02-12E	0.520	1.38	139.8	59.7	46.5	0.4	154	32.2	0.58	27.9	48.1 ± 2.9
V02-02-12F	0.436	2.25	145.2	32.9	46.7	0.2	153	41.7	0.70	23.5	33.6 ± 2.0
V06-02-12A	0.058	1.23	13.8	11.5	28.1	0.8	17	36.7	0.63	28.5	45.3 ± 2.7
V06-02-12B	0.250	1.14	39.7	12.4	5.2	0.3	43	35.6	0.65	40.0	66.6 ± 4.0
V06-02-12C	0.056	0.94	5.6	27.1	24.8	4.9	12	33.2	0.60	38.0	63.3 ± 3.8
V06-02-12D	0.125	0.44	26.7	64.5	78.0	2.4	42	28.2	0.60	24.2	40.4 ± 2.4
V06-02-12E	0.070	1.24	4.1	3.8	7.5	0.9	0.9	33.9	0.64	88.0	137.6 ± 8.3[a]
V07-02-12A	0.256	1.65	63.1	105.2	31.6	1.7	88	43.5	0.66	24.0	36.4 ± 3.5
V07-02-12B	0.258	1.10	69.8	137.3	44.7	2.0	103	41.9	0.69	20.8	30.1 ± 4.3
V07-02-12C	0.249	0.85	79.7	135.2	42.3	1.7	112	41.9	0.64	18.4	28.7 ± 3.0
V07-02-12D	0.169	0.80	70.7	89.6	28.2	1.3	92	35.4	0.60	15.2	25.3 ± 4.9
V07-02-12E	0.146	2.78	50.5	85.8	25.9	1.7	71	51.5	0.73	17.0	23.3 ± 2.3

Notes: Crystal weight has been determined using the Ca content. eU: effective uranium, Rs: equivalent spherical radius; F_T: the α-ejection correction after Ketcham et al. (2011).

[a] Ages are those excluded for the discussion due to suspected implantation (see text).

(ii) thermochronological data (apatite fission-track and (U-Th-Sm)/He analyses) as derived from regional sampling.

Our work provides new insights into the uplift and morphotectonic evolution of the Admiralty Mountains sector of the TAM and its relationships to geodynamic models.

2. Geological background

The TAM are the largest non-compressional mountain range on Earth. The bedrock of the TAM in the Ross Sea region is composed of the exhumed roots of the late Neoproterozoic to early Paleozoic Ross Orogen

(Stump, 1995). In NVL, three major post-Paleozoic structural domains can be distinguished (Tessensohn, 1994): the Outback Shoulder, inland to the west, the Rennick Graben, in the middle and traversing NVL from NW to SE and the Admiralty Block to the east (Fig. 1a). The Rennick Graben is a tectonic depression bounded by complex array of Cenozoic dextral and normal faults (Rossetti et al., 2003). The Admiralty Block (the Bowers and Robertson Bay terranes assembly; Tessensohn, 1994; Rossetti et al., 2006a) has a triangular shape and on one side forms the eastern shoulder of the Rennick Graben. The Lanterman Fault (Fig. 1a) is a major topographic and structural boundary separating the westward Neoproterozoic–Early Paleozoic Wilson Terrane from the Admiralty Block to the east. South of the Lanterman Fault, a major sub-horizontal erosional unconformity (the Kukri peneplane) separates the exhumed roots of the Ross Orogen, below, to the Devonian–Triassic Beacon sandstones and the early Jurassic Ferrar dolerites, above (Barret, 1991). North of the Lanterman Fault, the Admiralty Block landscape is characterized by an Alpine-type morphology shaped by narrow valleys and sharp cliffs with peaks reaching altitudes of more than 4000 m in the Admiralty Mountains (Mount Minto) (Armienti and Baroni, 1999; Van der Wateren et al., 1999; Baroni et al., 2005). The Cenozoic McMurdo Volcanic Group (e.g., Jordan, 1981; McIntosh and Kyle, 1990; Rocchi et al., 2002) includes N–S elongated shield volcanoes exposed for a distance of >200 km from Coulman Island to Cape Adare and the Hallet Peninsula (Hallett Volcanic Province) (Fig. 1a and b). This volcanic field was active during the Middle Miocene to Quaternary (from 14 Ma up to 1 Ma; Läufer et al., 2006, and references therein; Mortimer et al., 2007).

At regional scale, the Cenozoic tectonic setting is dominated by a set of major NW-SE dextral strike-slip faults (Fig. 1a), as the Lanterman, Aviator, Campbell, Priestley faults, that crosscut the western shoulder of the Ross Sea (Wilson, 1995; Salvini et al., 1997; Rossetti et al., 2003, 2006b; Storti et al., 2007). Wrench tectonics started during the Eocene (at about 35–40 Ma; Rossetti et al., 2003, 2006b), but structural observation and offshore seismic lines indicate reactivation up to recent time (Stackebrandt, 2003; Rossetti et al., 2006b; Storti et al., 2007). Cenozoic strike-slip faults are abutted by N–S-striking basins in the Ross Sea along the entire western Ross Sea margin (Salvini et al., 1997; Hamilton et al., 2001; Storti et al., 2001). Sedimentary records and seismic lines reveal Paleogene-Early Miocene subsidence episodes in most of these basins, e.g. Adare Basin, Victoria Land Basin, and Northern Basin (Fig. 1a) (see Davey and De Santis, 2005; Davey et al., 2006). In the Adare basin, stretching led to continental break-up, with about 170 km of ENE-WSW oceanic spreading from 43 Ma to 26 Ma (Cande et al., 2000; Cande and Stock, 2004).

The uplift and erosion history of the whole Admiralty Block is considered to be mainly Cenozoic (Fitzgerald and Gleadow, 1988; Lisker, 2002). Previous apatite fission-track studies from northern Admiralty Block gave ages between 125 Ma and 40 Ma showing a strong correlation with elevation: ages increase and mean track lengths decrease with increasing elevation (Fitzgerald and Gleadow, 1988; Lisker, 1996, 2002). Following Baroni et al. (2005), the valley networks of the Admiralty Mountains can be ascribed to fluvial origin. A well-developed alpine topography postdates the previously sculpted fluvial morphology. According to Baroni et al. (2005), temperate glaciers were responsible for denudation until the late Miocene and probably exhumed the youngest intrusive rocks cropping out in the coastal areas (19 Ma crystallization age; Rocchi et al., 2002).

The study area is located in the Admiralty Mountains region (Fig. 1a and b), within the Admiralty Block (Fig. 1). Bedrock of the study area is made up of Precambrian–Cambrian turbidite-dominated deposits of the Robertson Bay Terrane that is locally intruded by Devonian–Carboniferous Admiralty Intrusives (GANOVEX Team, 1987). The Admiralty Mountains region exposes a NW–SE-trending belt of sub-vertical rock panels, dominantly structured during the Early Palaeozoic accretionary complex formation at the palaeo-Pacific active margin of Gondwana (Rossetti et al., 2006a). The Cenozoic tectonic scenario of the Admiratly Mountains region is controlled by distributed and interfering NE-SW extensional and NW-SE dextral fault strands, which are recognised to be active concurrently with and to exert the control on the activity of the Mc Murdo Volcanic Group (Faccenna et al., 2008).

3. Topography of the Admiralty Mountains area

3.1. Methodology

Topography is the integrated result of climatically-induced erosion and tectonic rock uplift, and hence provides clues about deep seated geodynamic processes. We performed a numerical analysis of the digital elevation model Bedmap2 produced by the British Antarctic Survey (Fretwell et al., 2013). Bedmap2 is a grid of uniform 1-km spacing surface elevation, ice-thickness, sea-floor and subglacial bed elevation derived from a variety of topographic and geophysical sources. (Fig. 2a). The numerical data and visualisation processing was done with QGIS software. The different contribution of tectonics and erosion to the topography can be investigated through the analysis of local relief, being the result of erosional processes acting to destroy relief that is building up or has already been built by tectonic processes. Local relief is defined by the difference in height in a region between the peaks of highest elevation and the valley bottoms and is computed through the definition of summit and base level maps (Kühni and Pfiffner, 2001 and references therein) (Fig. 2).

Summit and base level maps contain the points of highest and lowest elevation, respectively, within a given area. The maps were computed by dividing the Bedmap2 into squares of equal size (20 km ×20 km). This grid dimension was chosen to smooth local irregularities caused by incision of glaciers. The coordinates of the point of highest and lowest elevation are stored. New surfaces containing these points are computed.

3.2. Topography of the Admiralty Mountains area

The summit level map of the Admiralty Mountains shows regions of maximum elevation similar to the Bedmap2 (Fig. 2a and b). The base-level map shows approximately the same distribution for the maximum elevations as the summit level map (Fig. 2b and c).

By subtracting the base-level elevations from the summit level elevations a local (or residual) relief map was obtained (Fig. 2d). In the Admiralty Mountains, our computed local relief map reveals that almost the entire study area shows values between 1500 m and 2500 m, which are high compared to other mountains worldwide and alpine incised landscapes (Kühni and Pfiffner, 2001). A band 180 km long and 70 km wide of very high local relief (>2500 m) extends NNE to SSW almost parallel to the coast (Fig. 2d). The region inland of this very high local relief area, is almost contained in the isopleth of local relief >2000 m, revealing that, in the Admiralty Mountains, high amounts of erosion are evident up to ca. 200 km inland from the coast, and with similar amount of erosion distributed across an area of 10,000 km^2.

3.2.1. Morphometry in profile view

The summit level, base-level and local relief maps are compared to three swath profiles showing maximum, mean and minimum elevation over a band ca. 10 km wide (Fig. 2e), extracted orthogonal to the rift margin. The locations of the profiles are given in Fig. 2a. The profiles extend from the coast to more than ca. 150 km inland. Profile A and B start from the divide between the upper Tucker glacier, flowing toward the east, and Lillie and Ebbe Glaciers (Fig. 2), flowing towards the north-west. The two southern profiles show the coastal massifs formed by the Cape Hallett and Daniell shield volcanoes. From inland to the coast, the topography increases from the divide (that does not match with highest elevation), it reaches its maximum elevation (up to 4000 m) about 50 km from the coast (around Mt Minto) and then decreases toward the coast. The difference between the maximum and minimum elevation envelopes is higher toward the coast, up to ca. 50–70 km inland and along the intermediate swath profile B; and tends to

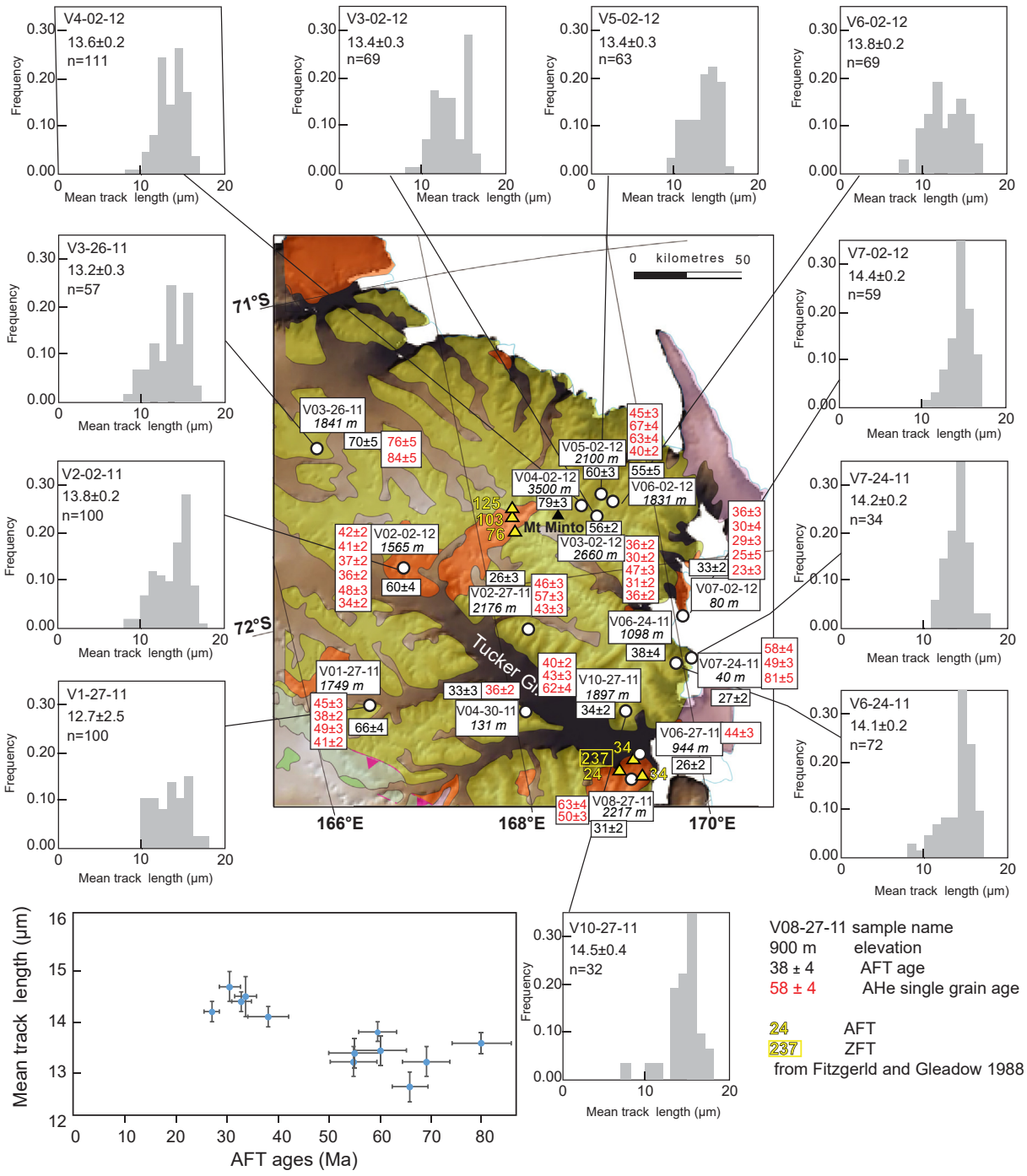

Fig. 4. Simplified geological map from Fig. 1 with AFT and AHe age data. Track length distributions and AFT vs. mean length plot are also shown.

decrease towards north and south along swath profiles A and C, confirming the location of highest local relief (>2500 m) outlined by the local relief map (Fig. 2d).

The three profiles show that Admiralty Mountains topography differs from the rest of the TAM, where topography typically increases from inland towards the coast and a steep escarpment separates the summit from a low topography coastal region (e.g. Olivetti et al., 2018), common to the general trend of passive margins. The topography of the Admiralty Mountains region is a ca. 200 km wide dome with maximum elevation more than 50 km from the coast (Fig. 2e). Even if the maximum elevation is far from the coast, the eastern seaward margin is characterized by an abrupt decrease in topography of 2000 m in just a few kilometres (Fig. 2e).

4. Structural analysis

4.1. Methods

Structural analysis was performed to understand the style and kinematics of faults in relation to the regional distribution of the apatite fission-track (AFT) and (U–Th)/He (He) ages (see below). Structural data on faults, kinematic indicators, and joints were measured at nineteen field sites, distributed between the coastal region and 150 km inland (Fig. 3). A total of 75 fault plane orientations and corresponding slickenlines were measured. Characterization of the brittle fabrics and fault kinematics was based on classical criteria (e.g., Petit, 1987; Doblas, 1998), complemented by recognition of geological offsets in the field.

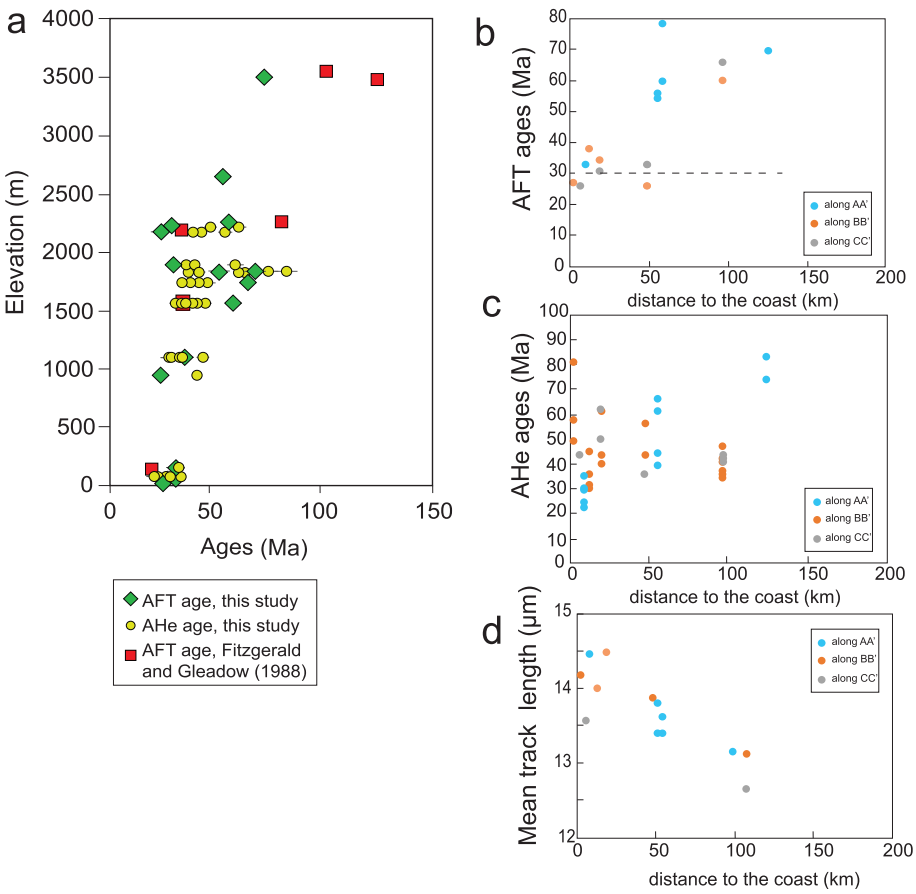

Fig. 5. AFT, AHe ages and Mean Track Length trends: (a) Age-Elevation Relationship; (b) AFT ages vs. distance from the coast, along the three profiles of Fig. 2a; (c) AHe ages vs. distance from the coast; (d) Mean track length vs. distance from the coast.

The fault and fracture population analysis was performed using Daisy software (http://host.uniroma3.it/progetti/fralab/).

4.2. Brittle deformation pattern

Structural investigation was carried out over the entire Admiralty Mountains region, till a distance of 150 km from the coast (Fig. 3). These new data complement those of Faccenna et al. (2008), focused mainly along the coastal region. Collected 106 fault and joint data (strike, dip, slickenlines, kinematics) provided two main, sub-vertical and nearly orthogonal orientation clusters, striking NW-SE to WNW-ESE strikes and NE-SW, respectively (Fig. 3).

In the field, the deformation is always diffuse and no major rift-basin boundary faults were recognised in the field, in agreement with all of the previous field studies along the TAM front (Wilson, 1995; Rossetti et al., 2006a; Storti et al., 2008). Metamorphic sandstones and argillites of the Robertson Bay Terrane does not provide good markers to unravel fault kinematics and geometries that are often subparallel to vertical closely-spaced bedding. Measured faults show small displacements of geological markers that are usually of order of millimetres to centimetres. A systematic array of fractures is commonly observed perpendicular to bedding (Fig. 3).

Structural data collected in the Admiralty Intrusives are dominated by sub-vertical NW–SE oriented joint and fault networks. Fault kinematics is dominated by dextral strike-slip (pitch-angle of the slickenlines ranging 0°–45°) movements (sites 51–52 and 66 in Fig. 3). Data from the Robertson Bay Terrane rocks show very similar geometry and kinematics than those from Admiralty Intrusives: (i) a NE–SW striking population of sub-vertical joints and faults with dextral strike–slip kinematics (e.g. sites 17–15 field picture in Fig. 3) and (ii) a NW–SE oriented joints and faults that rework the vertical bedding planes showing some horizontal slickenlines (e.g. sites 53–54). Structural data collected in the McMurdo volcanic rocks (sites 38–68, 39, 50; field picture in Fig. 3) show irregular fault surfaces, dominated by NE–SW and WNW–ESE striking faults with few evident slickenlines (dominantly oblique). A minor number of faults show a NE–SW orientation; no slickenlines were detected.

In general, the two fault populations were observed at all of the sites. Northern sites close to the coast (sites 38–68, 50) have similar fault and fracture orientations to those at southern sites at ca. 150 km away (sites 59 and 66), and to those at central sites (sites 51–54). It is noteworthy that we observed similar fault and fracture orientations at sites located far from the coast in the internal portion of the Admiralty Mountains. In these sites (15, 17, 14, 46 in Fig. 3), where outcrops above ice are very limited, we observed common sub-parallel NW–SE striking fractures and faults with small offset (Fig. 3). We observed no correlation between structural orientation and rock type. McMurdo basalts dated at 10 Ma by Mortimer et al. (2007) (sites 38–68 in Fig. 3) are cut by the same two populations of brittle fractures (NW–SE and NE–SW oriented, respectively) found in the Robertson Bay Terranes rocks and Admiralty Intrusives (Fig. 3). As previously recognised by Faccenna et al. (2008), we did not observe a clear chronological relationship between the two structure populations.

5. Low-temperature thermochronology

5.1. Methods

The AFT partial annealing zone (PAZ) is 60–120 °C (Green and

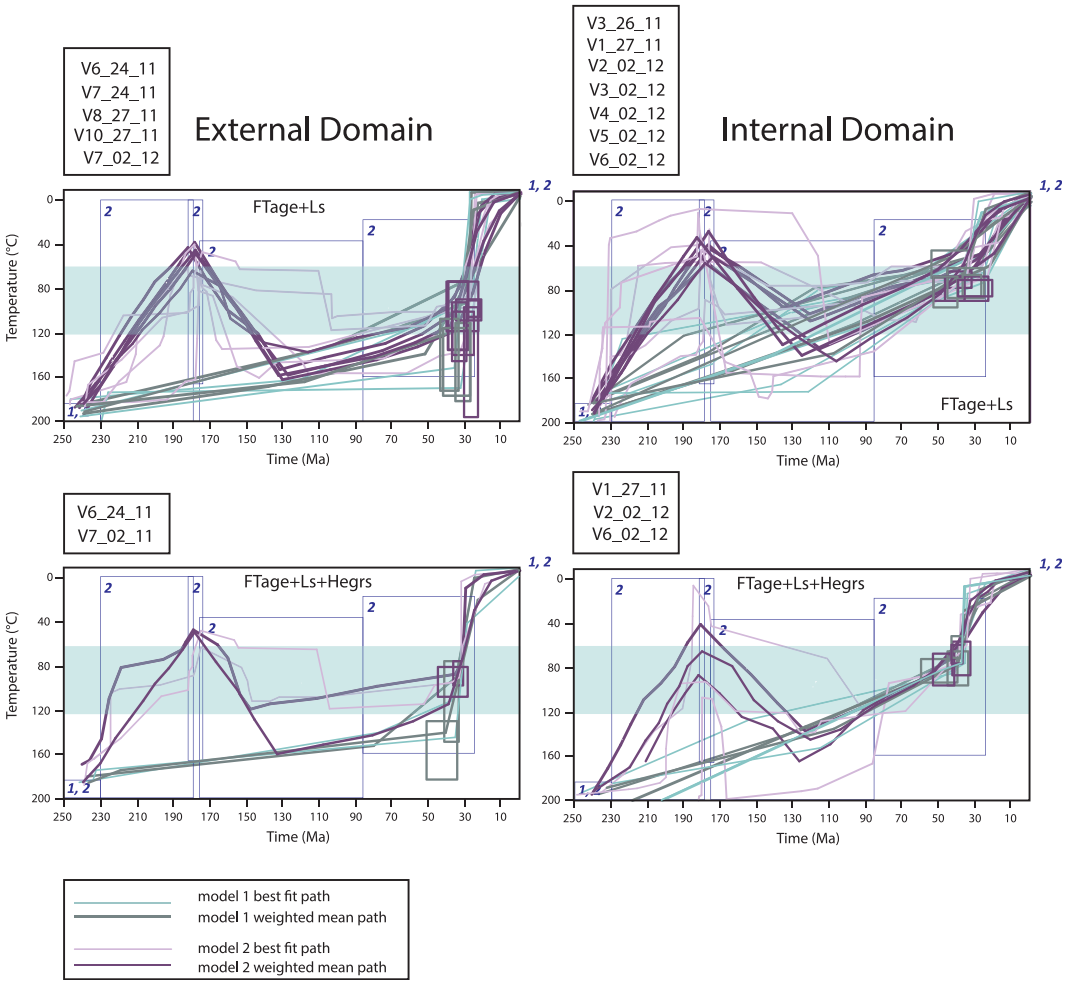

Fig. 6. HeFTy time – temperature thermal models. For each model, 100,000 random paths were tested. Best fit and weighted mean paths are reported for model 1 and 2 (blu boxes are the constraints for the two models) and for AFT age plus track lengths (Ls) model only and AFT age plus track lengths plus He single grain ages (Hegrs) model. Coloured thick boxes represent the range of time and temperature uncertainty of the onset of the Cenozoic cooling. For box dimensions see calculations in Table 3.

Duddy, 1989; Ketcham et al., 1999) and the AHe partial retention zone (PRZ) is 40–120 °C (Flowers et al., 2009; Gautheron et al., 2009), making the techniques useful to assess cooling history in the upper 3–5 km of the crust.

A total of 19 samples were collected from the Admiralty Intrusives and Robertson Bay Terrane for AFT and AHe thermochronometry but only 15 were suitable for dating. Our data are the first to be published including samples of Precambrian to Cambrian turbiditic sandstones and shales of the Robertson Bay formation. The apatite grains were recovered using standard crushing, sieving, washing, magnetic, and heavy liquid separation.

5.1.1. *Apatite fission-track analysis*

Apatite grains were mounted in epoxy resin, ground, and polished to expose internal mineral surfaces. Etching with 5 N HNO_3 at room temperature for 20 s revealed spontaneous fission tracks intersecting the apatite surface. Samples were covered with a uranium-free muscovite external detector and irradiated with thermal neutrons at the LENA (Laboratorio Energia Nucleare Applicata) Triga Mark II reactor at Pavia University, Italy. Induced fission tracks in the external detector were revealed by etching the mounts in 40% HF at room temperature for 40 min. The fission tracks were counted by the first author under a nominal magnification of 1250× on a Zeiss Axioskop equipped with a Kinetek automatic stage at the CNR-IGG Fission-Track laboratory. The Trackkey 4.2 Program was used for all AFT age calculations procedures (Dunkl, 2002). A chi-square (χ^2) test was carried out on the AFT single-grain age in order to test homogeneity of data (Galbraith, 1981). The probability of (χ^2) was calculated for each sample: if $P(\chi^2) > 5\%$ then the sample is assumed to be homogenous (Galbraith and Laslett, 1993). Three samples (* in Table 1) were analysed in a second time only for AFT analysis, at the fission-track laboratory of the Padua University (analyst Cattò) following a similar procedure to that one of the other samples, after being irradiated at the Radiation Center of the Oregon University.

5.1.2. *Apatite (U-Th-Sm)/He analysis*

Apatite (U-Th-Sm)/He analyses were carried out at GEOPS (University Paris Sud, France). Crystal dimensions were evaluated under a binocular microscope, and equivalent sphere radii (Rs) were calculated to represent the He diffusion domain (e.g. Gautheron and Tassan-Got, 2010). Ejection factors (FT) were determined using Monte Carlo simulation (Ketcham et al., 2011; Gautheron et al., 2012). Individual grains were examined twice in order to check for any unrecognised He-rich inclusions. U, Th, Sm and Ca concentrations were measured by isotopic dilution using an ICPMS-HR thermofisher ELEMENT XR. Apatite grains were dissolved in a HNO_3 solution spiked with ^{235}U, ^{230}Th, ^{149}Sm and ^{42}Ca. Durango apatite standards were analysed at the same time, to ensure data quality, and yielded ages of 31.0 ± 1.6 Ma, which is in agreement with published age of 31.4 ± 0.2 Ma (McDowell et al., 2005). The one-sigma error on each AHe age amounts to 8% and 25%, reflecting uncertainty in the ejection factor correction (F_T) that can be quite large

Table 3
Results of the thermal modeling for the two models.

Sample	AFT central age±1σ (Ma)	AHe corr. (Ma)	Thermal modeling	Model1							Model 2						
				Good	Acc.	Old	Onset of accelerated cooling (Ma)	Temp (°C)	WMP onset (Ma)	WMP temp (°C)	Good	Acc.	Old	Onset of accelerated cooling (Ma)	Temp (°C)	WMP onset (Ma)	WMP temp (°C)
V06_24_11	38 ± 4	36±2[A]	FT + Ls	0	15	40.1	33 ± 5	105 ± 29	28	71	0	133	39.6	31 ± 8	97 ± 22	36	87
EXTERNAL D.		30±2[B]	FT + Ls +	0	9	37.4	37 ± 5	110 ± 37	35	90	0	5	46.7	33 ± 2	88 ± 10	35	86
		47±3[C]	He4grs (A, B, D, E)														
		31±2[D]															
		36±2[E]															
V07_24_11	27 ± 2	58±3[A]	FT + Ls	330	1875	27.7	31 ± 5	140 ± 30	52	136	792	1775	28.1	28 ± 4	119 ± 21	36	117
EXTERNAL D.		50±3[C]															
		81±5[E]															
V03_26_11	70 ± 5	76±5[C]	FT + Ls	22	1214	85.7	43 ± 9	63 ± 12	42	53	56	939	93.0	38 ± 6	65 ± 9	50	66
INTERNAL D.		84±5[E]															
V01-27-11	66 ± 4	45±3[A]	FT + Ls	193	1041	98.9	28 ± 8	75 ± 9	22	56	160	103	178	30 ± 8	76 ± 9	49	81
INTERNAL D.		38±2[B]	FT + Ls +	0	5	95.8	40 ± 2	74 ± 14	40	77	0	16	82.	40 ± 2	80 ± 7	40	62
		49±3[C]	He4grs (A, B, C, E)														
		41±2[E]															
V08_27_11	26 ± 3	63±4[A]	Ft + Ls	403	2299	30.9	34 ± 6	143 ± 30	52	137	907	1923	30.5	31 ± 4	119 ± 19	35	102
EXTERNAL D.		50±3[B]															
V10_27_11	34 ± 2	40±2[A]	Ft + Ls	0	2	39.0	28 ± 1	92 ± 4	27	91	0	12	36.6	30 ± 4	97 ± 10	29	68
EXTERNAL D.		43±3[B]															
		62±4[C]															
V02_02_12	60 ± 4	42±2[A]	Ft + Ls	8 n.s.	120 n.s.	74.2	41 ± 5	83 ± 11	35	65	70 n.s.	509 n.s.	72.1	40 ± 5	79 ± 12	48	93
INTERNAL D.		41±2[B]	FT + Ls + He6grs	26	51	278	40 ± 6	82 ± 14	39	79	10	24	68.4	37 ± 5	72 ± 16	53	83
		37±2[C]	FT + Ls + He5grs														
		36±2[D]	(A, B, C, D, F)														
		48±3[E]															
		34±2[F]															
V06_02_12	55 ± 5	45±3[A]	FT + Ls	191 n.s.	1080 n.s.	81.2	35 ± 9	74 ± 14	29	57	221 n.s.	1159 n.s.	60.7	46 ± 6	81 ± 19	31	58
INTERNAL D.		67±4[B]	FT + Ls + He4grs	0	54	85.2	50 ± 11	83 ± 10	44	73	0	194	76.2	48 ± 5	84 ± 11	34	51
		63±4[C]	(A, B, C, D)														
		40±2[D]	FT + Ls +														
			He2grs (A, D)														
V07_02_12	33 ± 2	36±3[A]	FT + Ls	15 n.s.	35 n.s.	32.9	37 ± 6	145 ± 29	33	120	37 n.s.	109 n.s.	34.3	32 ± 3	121 ± 27	40	112
EXTERNAL D.		30±4[B]	FT + Ls + He5grs	0	5	41.5	42 ± 8	156 ± 29	40	143	0	356	43.2	36 ± 7	96 ± 15	37	116
		29±3[C]	(A, B, C, D, E)														
		25±5[D]	FT + Ls + He4gr														
		23±3[E]	(B, C, D,E)														
V3	56 ± 2	–	FT + Ls	1	21	85.8	28 ± 4	76 ± 4	22	47	12	125	81.3	30 ± 6	76 ± 5	26	57
INTERNAL D.																	
V4	79 ± 3	–	FT + Ls	0	74	114	60 ± 4	74 ± 4	59	76	21	86	107	38 ± 7	60 ± 26	33	52
INTERNAL D.																	
V5	60 ± 3	–	FT + Ls	39	215	87.0	32 ± 8	69 ± 11	26	55	57	254	92	32 ± 7	68 ± 11	44	72
INTERNAL D.																	

Note: Model 1: Only monotonic cooling. Model 2: Mesozoic reburial. For each sample what is modelled i.e. AFT age plus lengths only and AFT age plus lengths plus He single grain ages are reported in the column named "Thermal Modelling" (letters A, B, C, D, E in brackets refer to the specific single-grain AHe age included in the modelling). The number of good fit (Good) and acceptable (Acc.) fit paths found for each model are reported. The computed ranges of time and temperature uncertainty at the onset of the Cenozoic cooling are reported, too, together with the time temperature values at the inflection representing the Cenozoic rapid cooling for the weighted mean path (WMP). The range of time and temperature uncertainty at the inflection (i.e., onset of last rapid cooling) from 95% confidence band of t–T paths calculated by HeFTy (Ketcham, 2005). See text for explanation.

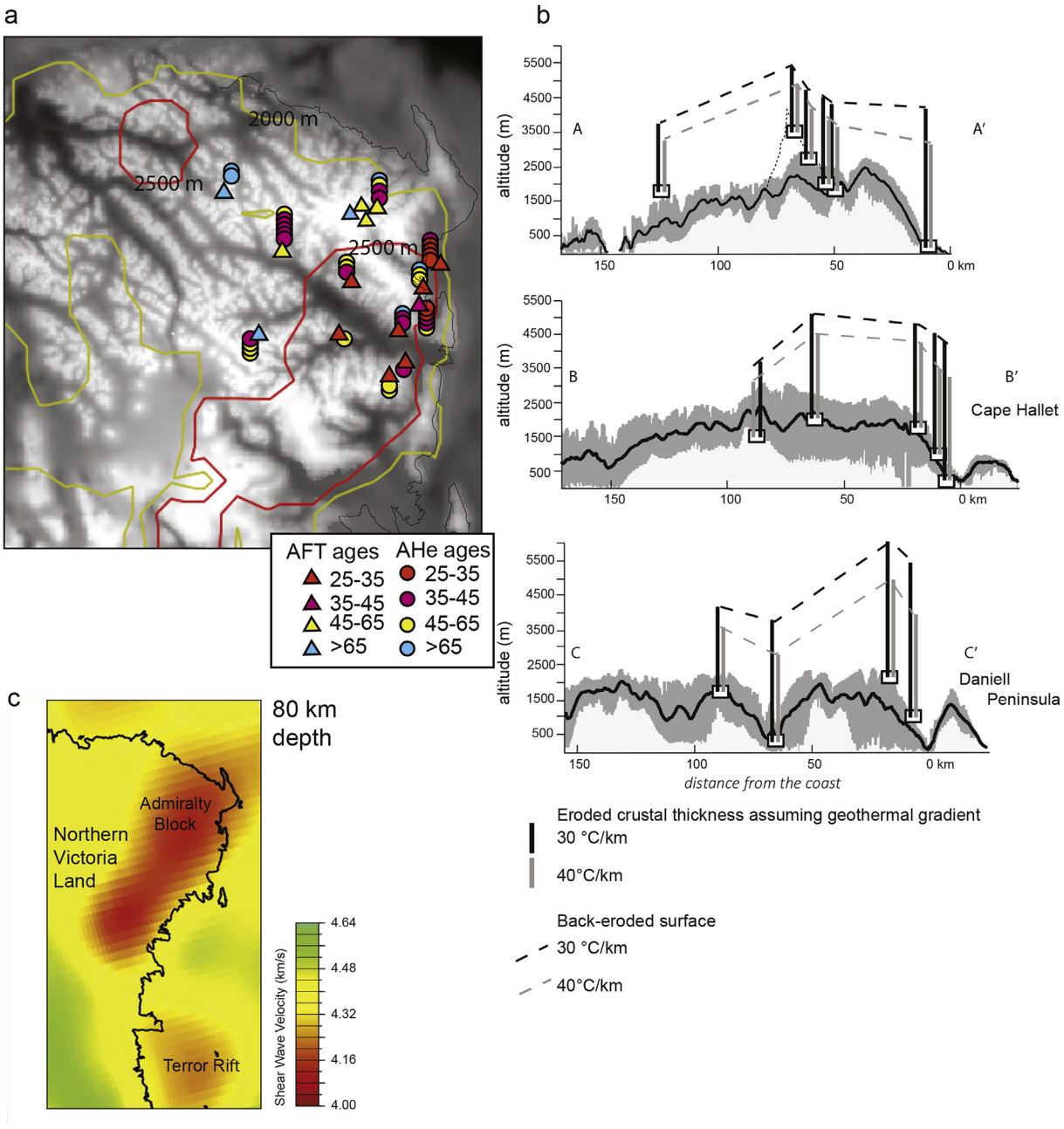

Fig. 7. (a) Local relief map of Fig. 2 with ranges of thermochronological ages reported on: see the coincidence between the younger ages (in red) and the area with the highest local relief (>2500 mm). (b) Swath profiles of Fig. 2 with the estimated amount of removed cover upon the analysed samples (rectangles) according to two different values for the paleo-geothermal gradient. Dashed envelopes are the reconstructed "back eroded" profiles according to two different values for the paleo-geothermal gradient. (c) Map of shear wave velocities at 80 km depth from Graw et al. (2016).

for smaller grains (Ehlers and Farley, 2003). Euhedral apatites were picked using a cross-polarized binocular microscope.

6. Results

AFT and AHe data are presented in Tables 1 and 2, respectively, and in Fig. 4. All ages are reported to one decimal place in Tables 1 and 2 but are rounded to whole numbers in text and figures. For the (U-Th-Sm)/He analysis, up to five single-grain aliquots were dated for each sample, thus (U-Th-Sm)/He analysis of apatite from the 12 samples resulted in 46 single grain ages. The (U-Th-Sm)/He data were carefully evaluated in order to detect possible outliers due to alpha implantation (Spiegel et al., 2009; Gautheron et al., 2012; Murray et al., 2014). Five aliquots that are statistically older than the other crystals have been certainly impacted by this phenomenon and are removed from further discussion. The excluded grains are reported in Table 2 with an asterisk.

AFT ages vary between 79 ± 3 Ma and 26 ± 3 Ma and mean track lengths range between intermediate to long values (12.3–14.7 μm) and moderate to large standard deviations (1.8–2.1 μm). Both ages and lengths show no correlation with Dpar (1.3–2.8 μm) (Table 1).

Single grain AHe ages range from 84 ± 5 Ma to 23 ± 2 Ma, with effective uranium (eU = U+0.24Th) content ranging from 5 to 273 ppm as shown in Table 2. Some samples present dispersed ages with some aliquots that are older than the central AFT age. Such a phenomenon has been previously documented (e.g., Wildman et al., 2016; Ketcham et al., 2018), and even along the TAM (Fitzgerald et al., 2006). The helium trapping model suggests that apatite becomes more He retentive with increasing radiation damage due to U and Th decay, resulting in an

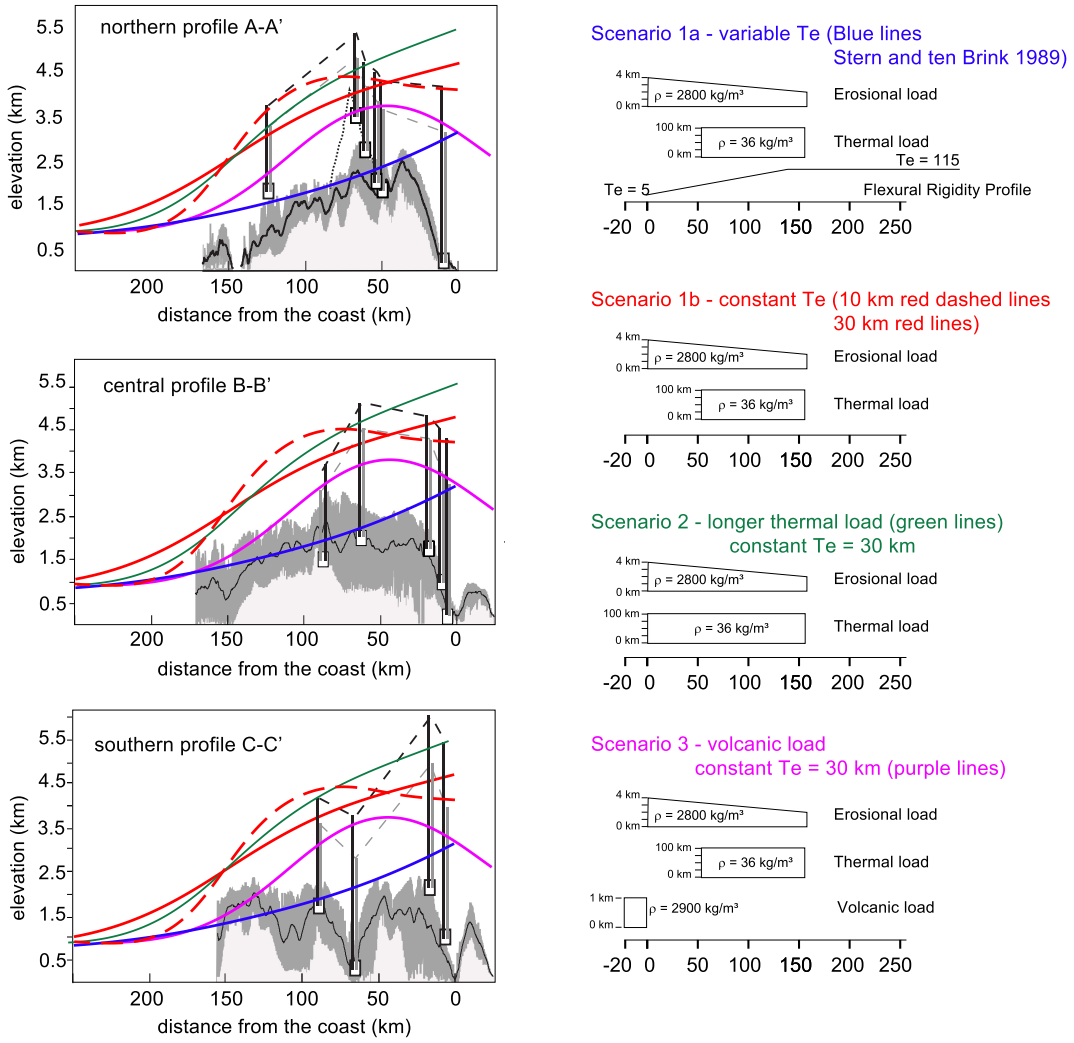

Fig. 8. Left column: swath profiles from Bedmap2 along the Admiralty Mountains region and modelled flexural profiles calculate through flex2D (Cardozo, 2016) applying different value of Te, different value and position of thermal loads. Right column: applied loads and flexural rigidity profile. The setup follows Stern and ten Brink (1989): "the densities and vertical scales for the various loads are different but the horizontal scale (distance) is the same, the magnitudes of the thermal and erosional loads are given as equivalent line loads."

increase of the closure temperature for helium retention in apatite and value higher than AFT (Shuster et al., 2006; Flowers et al., 2009; Gautheron et al., 2009) until a threshold where the closure temperature decreased (Recanati et al., 2017). In addition, some analysed apatite crystals are small, resulting in an increase of apatite geometry impact on He retention (Brown et al., 2013), perhaps compounded by other unquantified factors such as U, Th, and Sm zonation (Flowers and Kelley, 2011) and particularly apatite chemistry (Gautheron et al., 2013; Djimbi et al., 2015) due to the fact that most of the analysed rocks are metasediments likely containing apatites of different chemistry.

In the Admiralty Mountains area, the regional pattern of AFT ages shows a general tendency to the occurrence of older ages (79 Ma to 59 Ma) accompanied by shortened mean track length (MTL) (13.8–12.3 μm) in the interior, whereas the coastal domain is characterized by AFT ages clustering at 38–26 Ma with long MTL (Figs. 4 and 5b, c). However, differently from other regions of Victoria Land, the young ages are not confined to the coast at low elevation but they are found as far as 50–70 km inland and even at high elevation (i.e. samples V06_27_11, AFT age = 26 ± 2 Ma, elevation = 2176 m; Figs. 4 and 5b). In our study area, AFT ages are spatially separated into an external domain with ages <40 Ma even at high elevation, and an internal domain with older AFT ages. Single grain AHe ages cluster at 50–30 Ma, with a tendency to younger ages in the external domain (Figs. 4 and 5b).

AFT and AHe ages show a positive correlation with elevation in the interior (Fig. 5a). In the external domain there is no correlation between age and elevation. In Fig. 5a data from this study are complemented with data from Fitzgerald and Gleadow (1988) (see Fig. 4 for sample locations).

6.1. Thermal modelling

In order to reconstruct the low-temperature cooling history (T-t) of the study area, AFT and AHe data were modelled using HeFTy software v. 1.9.3 (Ketcham, 2005), which uses the Monte Carlo method to find T-t paths compatible with observed AFT and AHe data. The annealing model Ketcham et al. (2007) and the RDAAM radiation damage accumulation and annealing model (Flowers et al., 2009) were applied to AFT and AHe data, respectively.

AFT data and AHe single grain ages (when younger than the AFT ages) were combined and modelled together. In cases where adding (U-Th-Sm)/He data precluded the model from finding any good or acceptable path, those data were excluded. The thermal models are based on pre-existing geological and thermochronological information.

Fitzgerald and Gleadow (1988) reported zircon fission-track ages of 250–230 Ma and sphene fission-track ages around 300 Ma in the Admiralty Mountains area (Fig. 4). The zircon fission-track ages (closure

temperature: 250 ± 40 °C; Hurford, 1986) were used as starting point (250–230 Ma; 250–200 °C) in Model 1. Beacon sediments are not known in the whole Admiralty Block and in NVL elsewhere are only 300 m thick. Ferrar dolerites are not known in the Admiralty Block, too. We supposed slow cooling after a start at 250–230 Ma at ca. 200 °C, and the present-day surface temperature (ca. −10 °C) was used as the final constraint. A similar scenario, apart for the starting point, was envisaged to model AFT and AHe data in Terre Adélie, far to the east of our study area, by Rolland et al. (2019).

Model 2 was based on the studies of Prenzel et al. (2013, 2014, 2018) in the Deep Freeze Range (ca. 150 km south of our study area), where a kilometre-thick Jurassic – Eocene sedimentary sequence is inferred to have covered the region after shallow emplacement of Ferrar rocks, interpreted such as predominantly (sub-) volcanic sequence. Therefore, the underlying Beacon and basement rocks were at/near the surface at ~182 Ma. In Model 2, initial conditions comprise: (1) the same start as Model 1; (2) a long time period with a large temperature range until the Ferrar Event (230–180 Ma; 0–200 °C); (3) near surface temperatures for the Ferrar Event (185–175 Ma; 0–170 °C); (4) a subsequent temperature range implying a sedimentary overburden (180–85 Ma; 40–200 °C); (5) decreasing temperatures in the Cenozoic (66–25 Ma; 20–160 °C); (6) the present-day mean surface temperature (0 Ma; ca. −10 °C).

In Table 3, we report a summary of the tested thermal models. To obtain the range of time and temperature uncertainty of the onset of the Cenozoic cooling, we extracted the values of time and temperature at the inflection point representing the last rapid cooling for each good and acceptable path for each modelled sample and we calculated the mean and standard deviation values. The obtained ranges of values are reported in Table 3, together with the time and temperature values at the inflection for the weighted mean paths (WMP, Table 3). Results are summarized in Fig. 6.

Thermal modelling shows: (i) rapid cooling onset centred at 40–30 Ma, with a tendency to reduced cooling rates after 20–15 Ma, starting from temperatures higher or close to the bottom boundary of the PAZ for samples belonging to the external domain, and (ii) a complex history for the internal domain, where slow cooling or a long persistence within the PAZ predates rapid cooling from the upper part of the PAZ. For the internal domain, the onset-time of the last cooling phase is less well defined (Table 3, Fig. 6).

From the thermal modelling we infer that in the whole of our study area, the onset of the Cenozoic rapid exhumation phase is synchronous and that the difference between the external and internal domains is in the temperature of the inflection of the T-t trajectories. Therefore, the difference is in the thickness of the removed rock column, i.e. a deeper crustal level is exposed in the external domain. The internal domain, on the other hand, is the only portion of the study area recording the rock-history prior to the Cenozoic phase of cooling (see oldest modelled track in Table 3).

In general, samples gave a higher number of “good” and “acceptable” paths with Model 2, thus probably the scenario of protracted cooling is likely too simple and more complex thermal histories give better results. In the Admiralty Mountains, low temperature thermochronological ages are too young to either reject or support the presence of a Mesozoic basin postulated by Lisker and Läufer (2013) in this region.

7. Discussion

On the basis of the uniformity of topography and geological evolution along the TAM, the TAM uplift has been generally considered as produced by a unique process, underestimating the causes of regional variability. However, the Admiralty Mountains, in the northern tip of the TAM, is clearly a peculiar region for its Alpine-type morphology and for the absence of the Beacon and Ferrar/Kirkpatrick rocks widely cropping out throughout the continent.

In our study area, we recognize two domains: (i) an external domain with late Eocene–early Oligocene ages, similar to other sectors of the TAM front; and (ii) an internal domain characterized by a range of ages of 80–60 Ma. Although late Eocene–early Oligocene ages are found in other portions of the TAM, in the Admiralty Mountains, the young samples are found even at high elevation and the width of the young age domain is larger, it spans from the coast to 50–70 km inland. In the other sectors of the TAM, such young ages are limited to the TAM front, at low elevations, where maximum exhumation is focused and correspond to an area ca. 10 km wide (Fitzgerald, 1992), with a maximum of ca. 30 km (e.g. for the Royal Society Range; Olivetti et al., 2018).

Regional deformation of the Admiralty Mountains differs from the rest of the TAM mainly for the wideness of the involved area and for the fault pattern directions. In the Admiralty Mountains, NW–SE oriented dextral faults and NE–SW extensional faults are found across the entire studied area, even more than 100 km away from the coast (Fig. 3). In the rest of the TAM, faulting is focused along the range front and faults are very rare inland. Moreover, the two fault populations observed in the study area intersect each other orthogonally (see also Faccenna et al., 2008), differently from typical deformation at the TAM front that is dominated by localised oblique extension during the Cenozoic development of WARS (Wilson, 1995; Salvini and Storti, 1999; Rossetti et al., 2006b; Storti et al., 2006). Any possible explanation should take into account that in the Admiralty Mountains brittle Cenozoic faulting operated in a context with a significant structural inheritance at regional-scale (dominated by the penetrative NW–SE striking sub-vertical foliation of the Robertson Bay Terrane), whereas in the rest of the TAM, Cenozoic faulting mainly affected granitoids (thus nearly isotropic rocks). In this scenario, the nearly orthogonal fault patterns (NE–SW and NW–SE directed, respectively) can be interpreted either as two distinct phases of tectonic deformation, temporarily separated (Faccenna et al., 2008) or, alternatively, as produced synchronously as the consequence of orthogonal extension (with respect to the present-day coastline), accommodated by the NE–SW striking normal fault strands. In the latter case, the NW–SE fault strands are interpreted as minor transtensional dextral faults that operated through reactivation of the regional inherited NW–SE foliation. The latter hypothesis is supported by the linear array of the major volcanic edifices of the Cenozoic Mc Murdo Volcanic Group, trending sub-parallel to the coastline (Fig. 3), differently from other TAM sectors where the Mc Murdo volcanoess are more scattered. Furthermore, the alignment of the Hallet and Daniel volcanic edifices across the Tucker Glacier (Fig. 1) suggests a minor strike-slip movement along the Tucker Fault (Salvini et al., 1997) over the last 15 Ma.

7.1. Pre-Eocene exhumation

In the Admiralty Block, the absence of Beacon sandstones and Mesozoic basalts and dolerites provides an intriguing issue and a rare case throughout the TAM. Our thermochronological ages are too young to contain sound information on the pre-Eocene evolution, but the preservation of a single Triassic zircon fission-track age (Fitzgerald and Gleadow, 1988) suggests post-Triassic erosion was less than the thickness corresponding to the depth of the zircon PAZ (180–250 °C, e.g. Bernet, 2009; i.e. a depth to 6–8 km with a paleo-geothermal gradient of 30 °C/km). The existence of a Mesozoic sedimentary basin in Victoria Land (Lisker and Läufer, 2013) is not constrained by our data, which can also be modelled as consistent with long-lasting slow exhumation of Ross Orogeny basement. The post-Triassic cover thickness (Victoria Basin and basalt-dolerites) was likely thinner in the Admiralty Mountains than elsewhere in Victoria Land, and did not exceed 2 km, given our estimate of post-Eocene exhumation and the limit given by the preservation of a Triassic zircon and sphene fission-track ages in sample at low elevation (Fitzgerald and Gleadow, 1988). Thermal modeling for scenario 2 with post Jurassic burial suggests stagnation within the apatite PAZ and a possible but not well constrained exhumation from 130 Ma to 90 Ma. This age corresponds to the initial separation and spreading of the Antarctica and Australia plate (125 Ma to 90 Ma; Stagg and Willcox, 1992) and could be evidence for an Early Cretaceous uplift event, as

found in other parts of the TAM (Fitzgerald, 1992).

It is noteworthy that present crustal thickness in the Admiralty Mountains seems to attain about 40 km (Piana Agostinetti et al., 2005; Baranov and Morelli, 2013) against the 30 km of the neighbouring area (Hansen et al., 2016). The present crustal thickness is retained to be inherited since pre-Cenozoic times and therefore it is consistent with an already well developed pre-Cenozoic topography that underwent long-lasting erosion, and preventing Mesozoic sediment deposition.

7.2. Eocene-Oligocene to present topographic evolution

During the late Eocene-early Oligocene a phase of fast exhumation occurred, causing the removal of a crustal thickness of some km in the external domain (at least the entire apatite PAZ). Thermal modelling (Fig. 6) shows that rocks of the external domain at ca. 40 Ma had a temperature of 88–156 °C (depending on sample, Table 3) and they cooled between 26 Ma and 38 Ma through the apatite PAZ at a rate of about 6–4 °C/Myr. The temperature corresponding to the inflection of the modelled paths for the external domain (Fig. 6) can be transformed to crustal depth assuming a paleo-geothermal gradient. We assume values of 30–40 °C/km, higher with respect to the value of 25–30 °C/km previously inferred for NVL (Fitzgerald, 1994; Lisker et al., 2006), due to the presence of the recently detected low velocity zone below our sector of NVL (Graw et al., 2016). We obtained a thickness of removed crust of 2–5.2 km above the external domain (Fig. 7b). Thermal modelling suggests that at 40 Ma internal domain samples had a temperature of ca. 65–80 °C, corresponding to 1–2.3 km of crustal thickness. On the basis of these estimates, in Fig. 7b we reconstructed "back eroded" profiles, above the present-day topography.

There exists a spatial correlation between the present high local relief area and the area of maximum eroded thickness (i.e. younger thermochronological ages) (Fig. 7a). The high local relief area is also a high topography area (Fig. 7b), proving that the present local relief is due to a coupled effect of valley incision and uplift of the summit surface, and is not only an effect of higher glacial incision near the glacier mouth. The vertical distribution of AFT age (Fig. 4a) suggests a differential uplift between internal and external domains during the Cenozoic, causing external domain young samples to have even higher elevation than the older internal domain samples.

The internal domain local relief is $>$ 2000 m, such relatively high amount of erosion provides an explanation on why the internal domain does not show, in general, ages as old as $>$100 Ma. It corresponds to a substantial and similar amount of overburden removed above all the analysed samples of the internal domain. This is confirmed by the clustered values of temperature (narrow boxes, Fig. 6) at the time corresponding to the Cenozoic inflection of modelled thermal paths. We infer that the base level of the Admiralty Mountains represents the same exposed crustal level, with the exception of the external domain where it is at least 500 m deeper.

We suggest there may be a causal linkage between the Eocene-Oligocene high exhumation area, present high topography and high local relief, and a high-temperature anomaly in the upper mantle (Fig. 7c). This thermal anomaly is inferred from recent surface wave tomography (Graw et al., 2016). An anomalous hot upper mantle could support high topography through different mechanisms further discussed below, provoking deeper valley incision and hence high local relief. Its overlap (Fig. 7) with the region of young thermochronological ages suggests the thermal anomaly grew in the late Eocene–early Oligocene. This is in agreement with the hypothesis of Graw et al. (2016), who relates the origin of the anomaly to Cenozoic rifting of the Northern Basin. We note the large distance ($>$200 km) between the rifting of the Northern Basin and the location of the high topography and high temperature anomaly of the Admiralty Mountains region, while in southern Victoria Land the thermal anomaly exactly overlaps with the Terror Rift. This difference suggests an along strike variation of the lithosphere characteristics and style of deformation.

The contribution of a thermal anomaly to present topography, has been quantified by Brenn et al. (2017) in southern Victoria Land. They transformed the seismic waves velocity anomalies in a thermal load and insert it in the flexural model of Stern and ten Brink (1989) and ten Brink et al. (1997). Following a similar approach, we wanted to test if the uplift of the Admiralty Mountains region is consistent with a flexural model for a broken elastic lithosphere with imposed erosional and thermal loads and to test different values for the elastic thickness. For the erosional load calculation we used the removed crustal thickness estimated through our thermochronological analysis (see Fig. 7); for the thermal load we took the dimension (and location) of the low velocity anomaly from the tomographic image of Graw et al. (2016) and the density calculated in Brenn et al. (2017). We modelled the flexure using the Flex2D software package (Cardozo, 2016), the results of all the runs are reported in the Supplementary Fig. 1.

We tested three different scenarios (Fig. 8) with a constant erosional load represented by a trapezoid body of 2 km of thickness at 150 km inland and 4 km at the coast; the thermal load is represented by a rectangular body 100 km thick that in scenario 1 is located between 50 km and 150 km from the coast and in scenario 2 is located between the coast and 150 km. In the scenario 3 we evaluated a possible role of the load of the volcanic edifices along the coast.

For the first run, we used the configuration proposed by Stern and ten Brink (1989), and tested by Brenn et al. (2017), characterized by a linearly variable Te, corresponding to a value of 115 km at 130 km far from the edge and to 5 km at the edge (where the lithosphere is broken). The curve of flexural uplift (blue line, Fig. 8) is very different from our reconstructed back-eroded profiles suggesting that a similar configuration is not suitable for the Admiralty Mountains uplift. The curves with constant and smaller values of Te (10 km and 30 km, dashed and continue red lines) are the lines that better fit the convex shape of our back-eroded profiles. Scenario 2 with an erosional load distributed between 150 km and the coast tends to produce a too large uplift at the edge (with different and variable Te, too, Supplementary Fig. 1). The role of the volcanic load (scenario 3) is interesting because it tends to increase the bending of the lithosphere: with the same Te used for the scenario 1 (Te of 30 km) the curve is more convex.

In general, we note that the configuration of Stern and ten Brink (1989) is not appropriate to explain the uplift pattern of the Admiralty Mountains. In the Admiralty Mountains, Te should be remarkable thin and probably constant beneath the entire extension of the Admiralty Mountains. Taking into account the uncertainties on the load value and location, we infer that Te values of 10–30 km beneath the fully Admiralty Mountains region (to 150–200 km inland from the coast) are reasonable (Fig. 8). These values are significantly lower than what proposed by most of the authors for the other sectors of the TAM (Stern and ten Brink, 1989; Stern et al., 2005; Brenn et al., 2017). We propose that lower values for the elastic thickness of the Admiralty Mountains region are due to the peculiar thermal conditions of the lithosphere. The anomalous hot upper mantle, suggested by Graw et al. (2016), has modified the elastic properties of the Admiralty Mountains lithosphere, making it softer with respect to the expected East Antarctic craton lithosphere. With reference to the dynamic topography envisaged for the Admiralty Mountains by Faccenna et al. (2008), a thin elastic thickness could increase the contribution of the mantle dynamic to the topography.

7.3. Time-relationship between exhumation and faulting

In our study area, we found evidences of post 10 Ma (McMurdo volcanic rocks) faulting which is in agreement with Faccenna et al. (2008) and studies from other portions of the TAM front (Paulsen and Wilson, 2009; Vignaroli et al., 2015). On the other hand, the youngest thermochronological ages cluster around the late Eocene–early Oligocene. Thus, deformation continued after the main phase of exhumation. The synchronous onset of faulting and exhumation is poorly constrained,

too, along the entire TAM. Cenozoic faulting was certainly already active during Eocene–Oligocene, with offshore evidences such as cross-cutting of the RSU6 unconformity (Salvini et al., 1997) and subsidence and faulting of the Cape Roberts Basin (Hamilton et al., 2001), and with onshore evidences such as the Ar–Ar dating of pseudothachylite of Terra Nova bay (34 Ma) and Black Ridge (50–30 Ma) (Di Vincenzo et al., 2004, 2013) and the age of the syntectonic dikes within the Meander Intrusives (48–36 Ma; Rocchi et al., 2002). The large uncertainties on the RSU6 unconformity age and the limited fault dating leave open the possibility that faulting along the margin and offshore predates the phase of main exhumation and continues after that.

8. Conclusions

In the Admiralty Mountains region, an external domain (from the coast to 50–70 km inland) exhibits late Eocene–early Oligocene thermochronological ages, even at high elevation, and corresponds to an exhumation of 2–5.2 km. Differently from other portions of the TAM, in the Admiralty Mountains, this area of maximum exhumation is wider (until 70 km inland) and characterized by high elevation, and is opposed internally to a region with AFT ages between 80 Ma and 60 Ma recording an exhumation phase coeval to that one of the external domain but with a more limited (1.1–2.3 km) crustal unroofing. In the external domain, the spatial correlation between young thermochronological ages, high topography, high local relief and the low seismic velocity anomaly (Graw et al., 2016), points to a high temperature mantle anomaly supporting topography.

With the obtained constraints on the thickness of the rock column removed upon our samples, we calculated an erosional load and reconstructed back-eroded profiles on our study area. We tested different models of flexural uplift, taking into account the thermal load imposed by the presence of the thermal anomaly beneath the Admiralty Mountains. We found that the modelled flexural uplift profiles that better match our reconstructed back-eroded profiles are those ones with an effective flexural thickness (Te) constant and of intermediate values (30–20 km). We proposed that the mantle thermal anomaly positioned under the Admiralty Mountains changed the characteristics of the lithosphere, making it softer, and causing a flexural uplift with a convex profile i.e. widening inland the high-elevation/high-exhumation area. The extent of the area interested by brittle deformation and its kinematic and geometric uniformity over the entire study area is consistent with uniform lithospheric characteristics beneath the Admiralty Mountains region.

Declaration of competing interest

The authors declare that they have no known competing financial interests or personal relationships that could have appeared to influence the work reported in this paper.

Acknowledgements

The research was carried out in the framework of the research projects PDR2013/AZ2.07 (coordinated by F. Rossetti) and PNRA16_00263 (coordinated by V. Olivetti) funded by PNRA (Italian Research Program in Antarctica). We are warmly grateful for the logistics provided by the PNRA and ENEA-UTA (expedition leader: A. Della Rovere), and acknowledge the “Helicopters New Zealand (HNZ)” pilots (Carl and Dominic) and all colleagues sharing time in the Castle Rock remote camp and at the Italian base “Mario Zucchelli”. Donate Pace is thanked for his help in sample preparation. Rosella Pinna-Jamme is thanked for her help during the (U-Th-Sm)/He analysis. We thank the Museo Nazionale dell’Antartide (sez. Siena) for operational support.

Appendix A. Supplementary data

Supplementary data to this article can be found online at https://doi.org/10.1016/j.gsf.2020.01.018.

References

Armienti, P., Baroni, C., 1999. Cenozoic climatic change in Antarctica recorded by volcanic activity and landscape evolution. Geology 27 (7), 617–620.
Baranov, A., Morelli, A., 2013. The Moho depth map of the Antarctica region. Tectonophysics 609, 299–313.
Baroni, C., Noti, V., Ciccacci, S., Righini, G., Salvatore, M.C., 2005. Fluvial origin of the valley system in northern Victoria Land (Antarctica) from quantitative geomorphic analysis. Geol. Soc. Am. Bull. 117, 212–228. https://doi.org/10.1130/B25529.1.
Barrett, P.J., 1991. The Devonian to Jurassic Beacon Supergroup of the Transantarctic Mountains and Correlatives in Other Parts of Antarctica: the Geology of Antarctica. Clarendon Press, Oxford, pp. 120–152.
Bernet, M., 2009. A field-based estimate of the zircon fission-track closure temperature. Chem. Geol. 259 (3–4), 181–189. https://doi.org/10.1016/j.chemgeo.2008.10.043.
Bhandari, N., Bhat, S.C., Lal, D., Rajagoplan, G., Tamhane, A.S., Venka-Tavaradan, V.S., 1971. Fission fragment tracks in apatite: recordable track lengths. Earth Planet. Sci. Lett. 13, 191–199.
Bialas, R.W., Buck, W.R., Studinger, M., Fitzgerald, P.G., 2007. Plateau collapse model for the transantarctic mountains–West Antarctic Rift System: insights from numerical experiments. Geology 35, 687–690.
Bott, M.H.P., Stern, T.A., 1992. Finite element analysis of Transantarctic Mountain uplift and coeval subsidence in the Ross Embayment. Tectonophysics 201 (3– 4), 341–356.
Brenn, G.R., Hansen, S.E., Park, Y., 2017. Variable thermal loading and flexural uplift along the Transantarctic Mountains, Antarctica. Geology 45 (5), 463–466.
Brown, R.W., Beucher, R., Roper, S., Persano, C., Stuart, F., Fitzgerald, P., 2013. Natural age dispersion arising from the analysis of broken crystals. Part I: Theoretical basis and implications for the apatite (U–Th)/He thermochronometer. Geochem. Cosmochim. Acta 122, 478–497.
Cande, S.C., Stock, J.M., 2004. Pacific Antarctic-Australia motion and the formation of the maquarie plate. Geophys. J. Int. 157, 399–414. https://doi.org/10.1111/j.1365-246X.2004.02224.x.
Cande, S.C., Stock, J.M., Muller, R.D., Ishihara, T., 2000. Cenozoic motion between east and west Antarctica. Nature 404, 145–150. https://doi.org/10.1038/35004501.
Cardozo, N., 2016. Designer, OSXflex Version 4.3 Freeware Software for OSX for Macintosh, p. 356. www.ux.uis.no/~nestor/work/programs.html.
Chery, J., Lucazeau, F., Daignières, M., Vilotte, J.P., 1992. Large uplift of rift flanks: a genetic link with lithospheric rigidity? Earth Planet Sci. Lett. 112, 195–211.
Dalziel, I.W., 1992. Antarctica; a tale of two supercontinents? Annu. Rev. Earth Planet Sci. 20 (1), 501–526.
Davey, F.J., De Santis, L., 2005. A multi-phase rifting model for the Victoria Land Basin, western Ross Sea. In: Fütterer, D.K., Damaske, D., Kleinschmidt, G., Miller, H., Tessensohn, F. (Eds.), Antarctica: Contributions to Global Earth Sciences. Springer, New York, pp. 301–306.
Davey, F.J., Cande, S.C., Stock, J.M., 2006. Extension in the western Ross Sea region—links between Adare basin and Victoria Land Basin. Geophys. Res. Lett. 33, L20315. https://doi.org/10.1029/2006GL027383.
Djimbi, D.M., Gautheron, C., Roques, J., Tassan-Got, L., Gerin, C., Simoni, E., 2015. Impact of apatite chemical composition on (U-Th)/He thermochronometry: an atomistic point of view. Geochem. Cosmochim. Acta 167, 162–176.
Di Vincenzo, G., Rocchi, S., Rossetti, F., Storti, F., 2004. ^{40}Ar-^{39}Ar dating of pseudotachylytes: the effect of clast-hosted extraneous argon in Cenozoic fault generated friction melts from the West Antarctic Rift System. Earth Planet Sci. Lett. 223, 349–364. https://doi.org/10.1016/j.epsl.2004.04.042.
Di Vincenzo, G., Rossetti, F., Viti, C., Balsamo, F., 2013. Constraining the timing of fault reactivation: Eocene coseismic slip along a Late Ordovician ductile shear zone (northern Victoria Land, Antarctica). Geol. Soc. Am. Bull. 125 (3/4), 609–624. https://doi.org/10.1130/B30670.1.
Doblas, M, 1998. Slickenside kinematic indicators. Tectonophysics 295 (1–2), 187–197.
Dunkl, I., 2002. Trackkey: a Windows program for calculation and graphical presentation of fission track data. Comput. Geosci. 28 (1), 3–12.
Ehlers, T.A., Farley, K.A., 2003. Apatite (U–Th)/He thermochronometry: methods and applications to problems in tectonic and surface processes. Earth Planet Sci. Lett. 206 (1–2), 1–14.
Faccenna, C., Rossetti, F., Becker, T.W., Danesi, S., Morelli, A., 2008. Recent extension driven by mantle upwelling beneath the Admiralty Mountains (East Antarctica). Tectonics 27, TC4015. https://doi.org/10.1029/2007TC002197.
Fitzgerald, P.G., Gleadow, A.J.W., 1988. Fission-track geochronology, tectonics and structure of the transantarctic mountains in northern Victoria Land, Antarctica. Chem. Geol. 73, 169–198.
Fitzgerald, P.G., Sandiford, M., Barrett, P.J., Gleadow, J.W., 1986. Asymmetric extension associated with uplift and subsidence in the transantarctic mountains and Ross embayment. Earth Planet Sci. Lett. 81 (1), 67–78.
Fitzgerald, P.G., 1992. Tectonics and landscape evolution of the Antarctic plate since the breakup of Gondwana, with an emphasis on the west Antarctic Rift system and the transantarctic mountains. R. Soc. N. Z. Bull. 35, 453–469.
Fitzgerald, P.G., 1994. Thermochronologic constraints on post-Paleozoic tectonic evolution of the central Transantarctic Mountains. Antarctic. Tectonics 13 (4), 818–836.

Fitzgerald, P.G., Baldwin, S.L., Webb, L.E., O'Sullivan, P.B., 2006. Interpretation of (U–Th)/He single grain ages from slowly cooled crustal terranes: a case study from the Transantarctic Mountains of southern Victoria Land. Chem. Geol. 225 (1), 91–120.

Flowers, R.M., Ketcham, R.A., Shuster, D.L., Farley, K.A., 2009. Apatite (U–Th)/He thermochronometry using a radiation damage accumulation and annealing model. Geochem. Cosmochim. Acta 73, 2347–2365.

Flowers, R.M., Kelley, S.A., 2011. Interpreting data dispersion and "inverted" dates in apatite (U–Th)/He and fission-track datasets: an example from the US midcontinent. Geochem. Cosmochim. Acta 75, 5169–5186.

Fretwell, P., Pritchard, H.D., Vaughan, D.G., Bamber, J.L., Barrand, N.E., Bell, R., Bianchi, C., Bingham, R.G., Blankenship, D.D., Casassa, G., Catania, G., Callens, D., Conway, H., Cook, A.J., Corr, H.F.J., Damaske, D., Damm, V., Ferraccioli, F., Forsberg, R., Fujita, S., Gim, Y., Gogineni, P., Griggs, J.A., Hindmarsh, R.C.A., Holmlund, P., Holt, J.W., Jacobel, R.W., Jenkins, A., Jokat, W., Jordan, T., King, E.C., Kohler, J., Krabill, W., Riger-Kusk, M., Langley, K.A., Leitchenkov, G., Leuschen, C., Luyendyk, B.P., Matsuoka, K., Mouginot, J., Nitsche, F.O., Nogi, Y., Nost, O.A., Popov, S.V., Rignot, E., Rippin, D.M., Rivera, A., Roberts, J., Ross, N., Siegert, M.J., Smith, A.M., Steinhage, D., Studinger, M., Sun, B., Tinto, B.K., Welch, B.C., Wilson, D., Young, D.A., Xiangbin, C., Zirizzotti, A., 2013. Bedmap2: improved ice bed, surface and thickness datasets for Antarctica. Cryosphere 7, 375–393. https://doi.org/10.5194/tc-7-375-2013.

Galbraith, R.F., 1981. On statistical models for fission track counts. J. Int. Assoc. Math. Geol. 13 (6), 471–478.

Galbraith, R.F., Laslett, G.M., 1993. Statistical models for mixed fission track ages. Nucl. Tracks Radiat. Meas. 21 (4), 459–470.

Ganovex Team, 1987. Geological map of north Victoria Land, Antarctica, 1:500000 explanation notes. Geol. Jahrbuch Reihe B 66, 7–79.

Gautheron, C., Tassan-Got, L., Ketcham, R.A., Dobson, K.J., 2012. Accounting for long alpha-particle stopping distances in (U-Th-Sm)/He geochronology: 3D modeling of diffusion, zoning, implantation, and abrasion. Geochem. Cosmochim. Acta 96, 44–56.

Gautheron, C, Tassan-Got, L, 2010. A Monte Carlo approach to diffusion applied to noble gas/helium thermochronology. Chem. Geol. 273 (3–4), 212–224.

Gautheron, C.E., Tassan-Got, L., Barbarand, J., Pagel, M., 2009. Effect of alpha-damage annealing on apatite (U-Th)/He thermochronology. Chem. Geol. 266, 166–179.

Gautheron, C., Barbarand, J., Ketcham, R.A., Tassan-Got, L., van der Beek, P., Pagel, M., Pinna-Jamme, R., Coffignal, F., Fialin, M., 2013. Chemical influence on α-recoil damage annealing in apatite: implications for (U–Th)/He dating. Chem. Geol. 351, 257–267.

Graw, J.H., Adams, A.N., Hansen, S.E., Wiens, D.A., Hackworth, L., Park, Y., 2016. Upper mantle shear wave velocity structure beneath northern Victoria Land, Antarctica: volcanism and uplift in the northern Transantarctic Mountains. Earth Planet Sci. Lett. 449, 48–60.

Green, P.F., Duddy, I.R., 1989. Some comments on paleotemperature estimation from apatite fission tracks analysis. J. Petrol. Geol. 12, 111–114. https://doi.org/10.1111/j.1747-5457.1989.tb00224.x.

Hamilton, R., Sorlien, C.C., Luyendyk, P., Bartek, L.R., 2001. Cenozoic tectonics of the Cape Roberts rift Basin and transantarctic mountains front, southwestern Ross Sea, Antarctica. Tectonics 20, 325–342. https://doi.org/10.1029/2000TC001218.

Hansen, S.E., Kenyon, L.M., Graw, J.H., Park, Y., Nyblade, A.A., 2016. Crustal structure beneath the northern transantarctic mountains and wilkes subglacial basin: implications for tectonic origins. J. Geophys. Res. Solid Earth 121, 812–825. https://doi.org/10.1002/2015JB012325.

Hurford, A.J., 1986. Cooling and uplift patterns in the Lepontine Alps, South Central Switzerland and an age of vertical movement on the Insubric fault line. Contr. Min. Petr. 92, 413–427.

Hurford, A.J., 1990. Standardization of fission track dating calibration: Recommendation by the Fission Track Working Group of the IUGS Subcommission on Geochronology. Chem. Geol.: Isotope Geosci. Sect. 80, 171–178.

Jordan, H., 1981. Tectonic observations in the Hallet volcanic province, Antarctica. Geol. Jahrbuch Reihe B 41, 111–125.

Ketcham, R.A., 2005. Forward and inverse modeling of low-temperature thermochronometry data. Rev. Mineral. Geochem. 58 (1), 275–314.

Ketcham, R.A., Carter, A., Donelick, R.A., Barbarand, J., Hurford, A.J., 2007. Improved modeling of fission-track annealing in apatite. Am. Mineral. 5–6, 799–810.

Ketcham, R.A., Donelick, R.A., Carlson, W.D., 1999. Variability of apatite fission-track annealing kinetics: III. Extrapolation to geological time scales. Am. Mineral. 84 (9), 1235–1255.

Ketcham, R.A., Gautheron, C., Tassan-Got, L., 2011. Accounting for long alpha-particle stopping distances in (U-Th-Sm)/He geochronology: refinement of the baseline case. Geochem. Cosmochim. Acta 75, 7779–7791.

Ketcham, R.A., van der Beek, P., Barbarand, J., Bernet, M., Gautheron, C., 2018. Reproducibility of thermal history reconstruction from apatite fission-track and (U-Th)/He Data. G-cubed 19 (8), 2411–2436.

Kühni, A., Pfiffner, O.A., 2001. The relief of the Swiss Alps and adjacent areas and its relation to lithology and structure: topographic analysis from a 250-m DEM. Geomorphology 41 (4), 285–307.

Läufer, A., Kleindshmidt, G., Hejnes-Kunst, F., Rossetti, F., Faccenna, C., 2006. Geological Map of the Cape Adare Quadrangle, North Victoria Land, Antarctica, Scale 1:250.000, Fed. Inst. for Geosci. and Nat. Resour., Hannover, Germany.

Lawrence, J.F., Wiens, D.A., Nyblade, A.A., Anandakrishnan, S., Shore, P.J., Voigt, D., 2006. Crust and upper mantle structure of the Transantarctic Mountains and surrounding regions from receiver functions, surface waves, and gravity: implications for uplift models. G-cubed 7 (10). https://doi.org/10.1029/2006GC001282. Q10011.

LeMasurier, W.E., Thomson, J.W., 1990. Volcanoes of the Antarctic Plate and Southern Ocean, vol. 48. American Geophysical Union, Antarctic Research Series, Washington, D.C., 487 pp.

Lisker, F., 1996. Geodynamik des Westantarktischen Riftsystems basierend auf Apatit-Spaltspuranalysen Berichte zur Polarforschung, vol.198. Kamloth, Bremerhaven (1996), 108 pp (in German).

Lisker, F., 2002. Review of fission track studies in northern Victoria Land—passive margin evolution versus uplift of the Transantarctic Mountains. Tectonophysics 349, 57–73. https://doi.org/10.1016/S00401951(02)00046-X.

Lisker, F., Läufer, A.L., Olesch, W.M., Rossetti, F., Schäfer, T., 2006. Transantarctic Basin: new insights from fission track and structural data from the USARP Mountains and adjacent areas (Northern Victoria Land, Antarctica). Basin Res. 18, 497–520.

Lisker, F., Läufer, A.L., 2013. The Mesozoic Victoria Basin: vanished link between Antarctica and Australia. Geology 41, 1043–1046.

McDowell, F.W., McIntosh, W.C., Farley, K.A., 2005. A precise ^{40}Ar-^{39}Ar reference age for the Durango apatite (U-Th)/He and fission-track dating standard. Chem. Geol. 214, 249–263.

McIntosh, W.C., Kyle, P.R., 1990. Hallet Volcanic Province, in volcanoes of the Antarctic. In: LeMasurier, W.E., Thomson, J.W. (Eds.), Volcanoes of the Antarctic Plate and Southern Oceans. Antarct. Res. Ser.: Phys. Sci., vol. 48. AGU, Washington, D. C, pp. 26–47.

Mortimer, N., Dunlap, W.J., Isaac, M.J., Sutherland, R.P., Faure, K., 2007. Basal Adare volcanics, Robertson bay, north Victoria Land, Antarctica: late Miocene intraplate basalts of subaqueous origin. In: Abstracts of the 10th International Symposium on Antarctic Earth Sciences. University of California, Santa Barbara, pp. 26–31.

Murray, K.E., Orme, D.A., Reiners, P.W., 2014. Effects of U–Th-rich grain boundary phases on apatite helium ages. Chem. Geol. 390, 135–151.

Olivetti, V., Rossetti, F., Balestrieri, M.L., Pace, D., Cornamusini, G., Talarico, F., 2018. Variability in uplift, exhumation and crustal deformation along the Transantarctic Mountains front in southern Victoria Land, Antarctica. Tectonophysics 745, 229–244.

Paulsen, T.S., Wilson, T.J., 2009. Structure and age of volcanic fissures on mount morning: a new constraint on Neogene to contemporary stress in the west Antarctic Rift, southern Victoria Land, Antarctica. Geol. Soc. Am. Bull. 121 (7–8), 1071–1088.

Petit, J.P., 1987. Criteria for the sense of movement on fault surfaces in brittle rocks. Struct. Geol. 9, 597–608.

Piana Agostinetti, N., Roselli, P., Cattaneo, M., Amato, A., 2005. Moho-depth and subglacial sedimentary layer thickness in the wilkes basin from receiver function analysis. IASPEI. Gen. Assemb. 281–284.

Prenzel, J.D., Lisker, F., Balestrieri, M.L., Läufer, A., Spiegel, C., 2013. The Eisenhower Range, Transantarctic Mountains: a natural laboratory to evaluate qualitative interpretation concepts of thermochronological data. Chem. Geol. 352, 176–187.

Prenzel, J., Lisker, F., Elsner, M., Schöner, R., Balestrieri, M.L., Läufer, A.L., Berner, U., Spiegel, C., 2014. Burial and exhumation of the Eisenhower Range, Transantarctic Mountains, based on thermochronological, sedimentary rock maturity and petrographic constraints. Tectonophysics 630, 113–130.

Prenzel, J., Lisker, F., Monsees, N., Balestrieri, M.L., Läufer, A.L., Spiegel, C., 2018. Development and inversion of a Mesozoic basin in the Terra Nova bay, transantarctic mountains. Gondwana Res. 53, 110–128. https://doi.org/10.1016/j.gr.2017.04.025.

Recanati, A., Gautheron, C., Barbarand, J., Missenard, Y., Pinna-Jamme, R., Tassan-Got, L., Carter, A., Douville, E., Bordier, L., Pagel, M., Gallagher, K., 2017. Helium trapping in apatite damage: insights from (U-Th-Sm)/He dating of different granitoid lithologies. Chem. Geol. 470, 116–131.

Rocchi, S., Armienti, P., D'Orazio, M., Tonarini, S., Wijbrans, J.R., Di Vincenzo, G., 2002. Cenozoic magmatism in the western Ross embayment: role of mantle plume versus plate dynamics in the development of the west Antarctic Rift system. J. Geophys. Res. 107 (B9), 2195. https://doi.org/10.1029/2001JB000515.

Rolland, Y., Bernet, M., Van Der Beek, P., Gautheron, C., Duclaux, G., Bascou, J., Balvay, M., Héraudet, L., Sue, C., Ménot, R.P., 2019. Late Paleozoic Ice Age glaciers shaped East Antarctica landscape. Earth Planet Sci. Lett. 506, 123–133.

Rossetti, F., Lisker, F., Storti, F., Läufer, A., 2003. Tectonic and denudational history of the Rennick graben (north Victoria Land): implications for the evolution of rifting between east and west Antarctica. Tectonics 22 (2), 1016. https://doi.org/10.1029/2002TC001416.

Rossetti, F., Tecce, F., Aldega, L., Brilli, M., Faccenna, C., 2006a. Deformation and fluid flow during orogeny at the palaeo-pacific active margin of Gondwana: the early Palaeozoic Robertson bay accretionary complex (north Victoria Land, Antarctica). J. Metamorph. Geol. 24, 33–53.

Rossetti, F., Storti, F., Busetti, M., Lisker, F., Di Vincenzo, G., Läufer, A., Rocchi, S., Salvini, F., 2006b. Eocene initiation of Ross Sea dextral faulting and implications for East Antarctic neotectonics. J. Geol. Soc. 163, 119–126. https://doi.org/10.1144/0016-764905-005.

Salvini, F., Brancolini, G., Busetti, M., Storti, F., Mazzarini, F., Coren, F., 1997. Cenozoic geodynamics of the Ross Sea Region, Antarctica: crustal extension, intraplate strike-slip faulting and tectonic inheritance. J. Geophys. Res. 102, 24,669–24,696. https://doi.org/10.1029/97JB01643.

Salvini, F., Storti, F., 1999. Cenozoic tectonic lineaments of the Terra Nova Bay region, Ross Embayment, Antarctica. Glob. Planet. Sci. 23, 129–144.

Shuster, D.L., Flowers, R.M., Farley, K.A., 2006. The influence of natural radiation damage on helium diffusion kinetics in apatite. Earth Planet Sci. Lett. 249, 148–161.

Smith, A.G., Drewry, D.J., 1984. Delayed phase change due to hot asthenosphere causes Transantarctic uplift? Nature 309 (5968), 536.

Spiegel, C., Kohn, B., Belton, D., Berner, Z., Gleadow, A., 2009. Apatite (U-Th-Sm)/He thermochronology of rapidely cooled samples: the effect of He implantation. Earth Planet Sci. Lett. 285, 105–114.

Stackebrandt, W., 2003. Tectonic and isostatic controls on landscape evolution in Northern Victoria Land, Antarctica. Geol. Jahrbuch Reihe B 129, 152.

Stagg, H.M.J., Willcox, J.B., 1992. A case for Australia-Antarctica separation in the Neocomian (ca. 125 Ma). Tectonophysics 210, 21–32.
Stern, T.A., Baxter, A.K., Barrett, P.J., 2005. Isostatic rebound due to glacial erosion within the Transantarctic Mountains. Geology 33 (3), 221–224.
Stern, T.A., ten Brink, U.S., 1989. Flexural uplift of the transantarctic mountains. J. Geophys. Res. 94 (B8), 10,315–10,330.
Storti, F., Rossetti, F., Salvini, F., 2001. Structural architecture and displacement accommodation mechanisms at the termination of the Priestley Fault, northern Victoria Land, Antarctica. Tectonophysics 341, 141–161.
Storti, F., Rossetti, F., Salvini, F., Phipps Morgan, J., 2007. Intraplate termination of transform faulting within the Antarctic continent. Earth Planet Sci. Lett. 260, 115–126. https://doi.org/10.1016/j.epsl.2007.05.020.
Storti, F., Rossetti, F., Läufer, A.L., Salvini, F., 2006. Consistent kinematic architecture in the damage zones of intraplate strike-slip fault systems in North Victoria Land, Antarctica and implications for fault zone evolution. J. Struct. Geol. 28 (1), 50–63.
Storti, F., Balestrieri, M.L., Balsamo, F., Rossetti, F., 2008. Structural and thermochronological constraints to the evolution of the West Antarctic Rift System in central Victoria Land. Tectonics 27 (4). https://doi.org/10.1029/2006TC002066. TC4012.
Stump, E., 1995. The Ross Orogen of the Transantarctic Mountains. Cambridge Univ. Press, New York, 284 pp.
Studinger, M., Bell, R.E., Buck, W.R., Karner, G.D., Blankenship, D.D., 2004. Subglacial geology inland of the Trans-antarctic Mountains in light of new aerogeophysical data. Earth Planet Sci. Lett. 220, 391–408.
ten Brink, U.S., Stern, T.A., 1992. Rift flank uplifts and hinterland basins: comparison of the Transantarctic Mountains with the great escarpment of southern Africa. J. Geophys. Res. 97, 569–585.
ten Brink, U.S., Bannister, S., Beaudoin, B.C., Stern, T.A., 1993. Geophysical investigations of the tectonic boundary between East and West Antarctica. Science 261, 45–50.
ten Brink, U.T., Hackney, R.I., Bannister, S., Stern, T.A., Makovsky, Y., 1997. Uplift of the Transantarctic Mountains and the bedrock beneath the East Antarctic ice sheet. J. Geophys. Res. 102 (B12), 27,603–27,621.
Tessensohn, F., 1994. The Ross Sea region, Antarctica: structural interpretation in relation to the evolution of the southern ocean. Terra Antarctica 1, 553–558.
van der Beek, P., Cloetingh, S., Andriessen, P., 1994. Mechanisms of extensional basin formation and vertical motions at rift flanks: constraints from tectonic modeling and fission track thermochronology. Earth Planet Sci. Lett. 121, 417–433.
Van der Wateren, F.M., Dunai, T.J., Klas, W., Van Balen, R.T., Verbers, A.L.L.M., Herpers, U., 1999. Contrasting Neogene denudation histories of regions in the Transantarctic Mountains, northern Victoria Land, Antarctica, constrained by cosmogenic nuclide measurements. Global Planet. Change 23, 145–172. https://doi.org/10.1016/S09218181(99)00055-7.
Vignaroli, G., Balsamo, F., Giordano, G., Rossetti, F., Storti, F., 2015. Miocene-to-Quaternary oblique rifting signature in the western Ross Sea from fault patterns in the McMurdo volcanic Group, north Victoria Land, Antarctica. Tectonophysics 656, 74–90.
Wildman, M., Brown, R., Beucher, R., Persano, C., Stuart, F., Gallagher, K., Schwanethal, J., Carter, A., 2016. The chronology and tectonic style of landscape evolution along the elevated Atlantic continental margin of South Africa resolved by joint apatite fission track and (U-Th-Sm)/He thermochronology. Tectonics 35, 511–545.
Wilson, T.J., 1995. Cenozoic transtension along the transantarctic mountains-West Antarctic rift boundary, southern Victoria Land, Antarctica. Tectonics 14, 531–545.